UC Santa Barbara
UC Santa Barbara Previously Published Works

Title

Infrasonic propagation from the 2010 Eyjafjallajökull eruption: Investigating the influence of stratospheric solar tides

Permalink

https://escholarship.org/uc/item/28w593sz

Journal

Journal of Geophysical Research: Atmospheres, 117(D21)

ISSN

01480227

Authors

Green, D. N
Matoza, R. S
Vergoz, J.
et al.

Publication Date

2012-11-16

DOI

10.1029/2012JD017988

Peer reviewed

Infrasonic propagation from the 2010 Eyjafjallajökull eruption: Investigating the influence of stratospheric solar tides

D. N. Green,[1] R. S. Matoza,[2,3] J. Vergoz,[2] and A. Le Pichon[2]

[1] The stratospheric infrasound duct, formed between Earth's surface and altitudes of ~50 km, is sensitive to spatiotemporal variations in stratospheric wind speed and temperature. Infrasound recorded at long range from the 2010 summit eruption of Eyjafjallajökull volcano, Iceland, exhibits temporal variability correlated with diurnal stratospheric solar tidal wind speed variations. Between 18 and 28 April 2010, signal observations at stations BKNI, U.K. (range, 1745 km), and IS18, Greenland (range, 2285 km), exhibit prominent diurnal variations in infrasonic amplitude, bandwidth, back azimuth, and apparent speed, which we identify using the CLEAN spectral analysis algorithm for unevenly sampled time series. Results of 3-D acoustic ray tracing through operational atmospheric specifications indicate that tidal wind speed variations (with amplitudes of ~20 m/s) can generate diurnal variations in the proportion of the acoustic wavefield propagating within the stratospheric acoustic duct. Range-dependent meteorology is required; propagation modeling using averaged meteorological profiles fails to predict the leakage of acoustic energy out of the stratospheric acoustic duct at times of low observed signal amplitudes. Ray tracing correctly predicts the phase of the observed signal amplitude and apparent speed variations. Diurnal variability in ducting, combined with diurnal variations in ambient noise at the sensors, can explain the observed signal bandwidth variations. Back azimuth variations (observed only along the Eyjafjallajökull to BKNI path) are not predicted by 3-D ray tracing. Tidal variations have implications for models of infrasound array network detection capability and for studies that utilize amplitude and bandwidth measurements to make inferences about the acoustic source.

1. Introduction

[2] Infrasound propagation paths are predominantly controlled by the atmospheric temperature and horizontal wind structure [e.g., *Reed*, 1969; *Balachandran et al.*, 1971; *Drob et al.*, 2003, 2010]. Therefore, infrasound arrivals recorded at Earth's surface are increasingly being used to probe atmospheric structure and associated spatiotemporal variations [e.g., *Kulichkov and Bush*, 2001; *Kulichkov*, 2004; *Le Pichon et al.*, 2005a, 2010].

[3] Solar tides are global-scale oscillations of the atmosphere excited by absorption of solar radiation. These tides generate temporal variations in atmospheric temperature, density and wind speed which are dominated by diurnal and semidiurnal oscillations [e.g., *Lindzen and Chapman*, 1969; *Forbes and Groves*, 1990; *Forbes*, 1990]. Diurnal and semidiurnal tides are primarily excited through insolation absorption by tropospheric water vapor (0–15 km altitude) and stratospheric/mesospheric ozone (40–60 km) respectively [*Forbes*, 1987]. From these source regions the oscillations propagate upward, increasing in amplitude with decreasing atmospheric density. The diurnal tidal wind is of importance between altitudes of 50 to 90 km, whereas the semidiurnal tidal wind is the most regular and largest amplitude component above altitudes of 80 km [*Donn and Rind*, 1972].

[4] Studies of infrasonic energy returned from the thermosphere clearly identify the effects of the high-amplitude semidiurnal tide at these altitudes [e.g., *Donn and Rind*, 1972; *Le Pichon et al.*, 2005b; *Assink et al.*, 2012]. In contrast, the influence of stratospheric tides on infrasound propagation has proven difficult to observe. Only low-amplitude diurnal variations in microbarom signal amplitude [*Donn and Rind*, 1971, 1972] and diurnal variations in signal back azimuth and apparent velocity from eruptions of Yasur volcano [*Dalaudier et al.*, 2009] have been associated with solar tidal variations close to the stratopause. Given current spatially

[1]AWE Blacknest, Reading, UK.

[2]CEA/DAM/DIF, Arpajon, France.

[3]Now at Institute of Geophysics and Planetary Physics, Scripps Institution of Oceanography, University of California, San Diego, La Jolla, California, USA.

Corresponding author: D. N. Green, AWE Blacknest, Brimpton Common, Reading RG7 4RS, UK. (dgreen@blacknest.gov.uk)
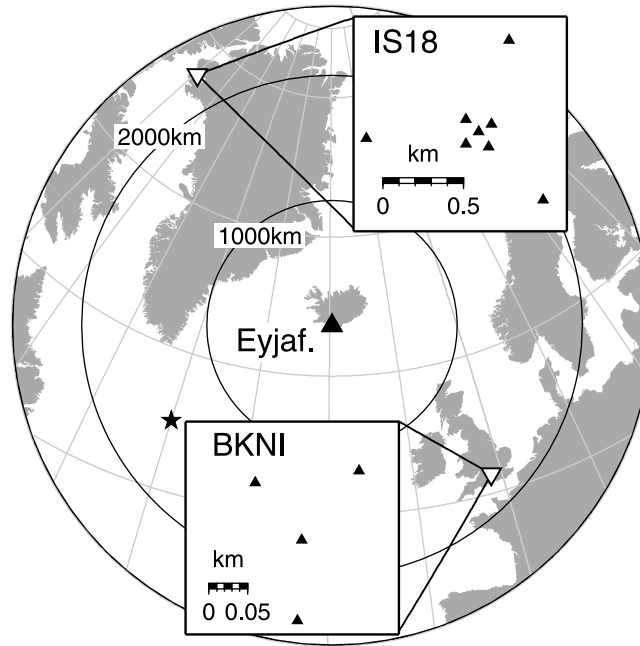
Figure 1. The location of the infrasound arrays, BKNI, UK, and IS18, Greenland (white inverted triangles), and the Eyjafjallajökull volcano, Iceland (black triangle). The insets show the configuration of the arrays, with each microbarometer location represented by a black triangle. The black star represents the approximate location of the microbarom source active in late April 2010, found by cross bearings. The map is an azimuthal equidistant projection, for which distances and bearings from the center point (Eyjafjallajökull) remain true. See *Matoza et al.* [2011a] for a full list of infrasound stations that detected this eruption.

sparse infrasound sensor networks, it is difficult to collect temporally dense stratospheric arrival time series from energetic, repetitive sources whose location and origin times are known. In addition, wind speed and temperature variations caused by atmospheric tides in the stratosphere exhibit lower amplitudes (5 to 15 m/s wind speed and <1 K temperature variations) and greater spatial variability than those in the mesosphere and lower thermosphere (up to 35 m/s wind speed and ∼25 K temperature variations) [*Forbes and Groves*, 1990; *Forbes*, 1990]. Therefore, it is expected that using acoustic sounding methods to study stratospheric tides will be more difficult than similar studies of thermospheric tides.

[5] This paper focuses on diurnal variations observed in infrasound detection parameters (signal amplitude, back azimuth, apparent speed, and mean frequency) for signals generated by the April and May 2010 eruption of Eyjafjallajökull volcano (63.63°N,19.62°W), Iceland. The summit eruption of Eyjafjallajökull began on 14 April 2010; highly explosive activity during the next 3 days generated an ash plume that extended up to altitudes of 9.5 km above sea level (asl) [*Gudmundsson et al.*, 2010]. This was followed by a period (18 April 2010 to 30 April 2010) of reduced eruption intensity and ash production while lava effusion began under the outlet glacier. Explosive activity resumed in early May, again generating ash plumes up to nine kilometers high. Due to the unusually persistent anticyclonic weather pattern to the south of Iceland the ash dispersal occurred mainly to the south and southeast, causing major disruption to commercial air traffic over Europe [e.g., *Petersen*, 2010; *Petersen et al.*, 2012].

[6] Infrasound generated by Eyjafjallajökull was recorded on 14 microbarograph arrays at ranges of up to 3666 km [*Matoza et al.*, 2011a]. Two stations, BKNI in the UK and IS18 in Greenland (Figure 1), recorded quasi-continuous infrasound signals from the eruption during 18 April 2010 to 28 April 2010. This paper focuses on temporal variations in signal characteristics (sections 2 and 3) and on identifying the mechanism for observed diurnal variations using acoustic propagation modeling (sections 4 and 5). It is shown that changes in acoustic ducting caused by stratospheric solar tidal motions can qualitatively explain many of the observed signal variations (section 6). This has implications for studies that use signal amplitudes and bandwidths to assess acoustic source parameters (section 7).

2. Observations

[7] The diurnal infrasound signal parameter variations are illustrated using data from two of the 14 stations that recorded the eruption: a 210 m aperture array, BKNI, located in the southern UK (51.364°N, 1.189°W), and a 1170 m aperture array, IS18, located in western Greenland (77.476°N, 69.288°W). These stations were chosen due to the quasi-continuous records at both locations with comparison to the other recording stations [*Matoza et al.*, 2011a, Figure 2] and the fact that they are located along approximately opposite trajectories from the source. BKNI is located 1745 km from Eyjafjallajökull with a receiver-to-source back azimuth of 328.6°, while IS18 is located at a range of 2286 km with a back azimuth of 104.3° (Figure 1 and Table 1). The larger
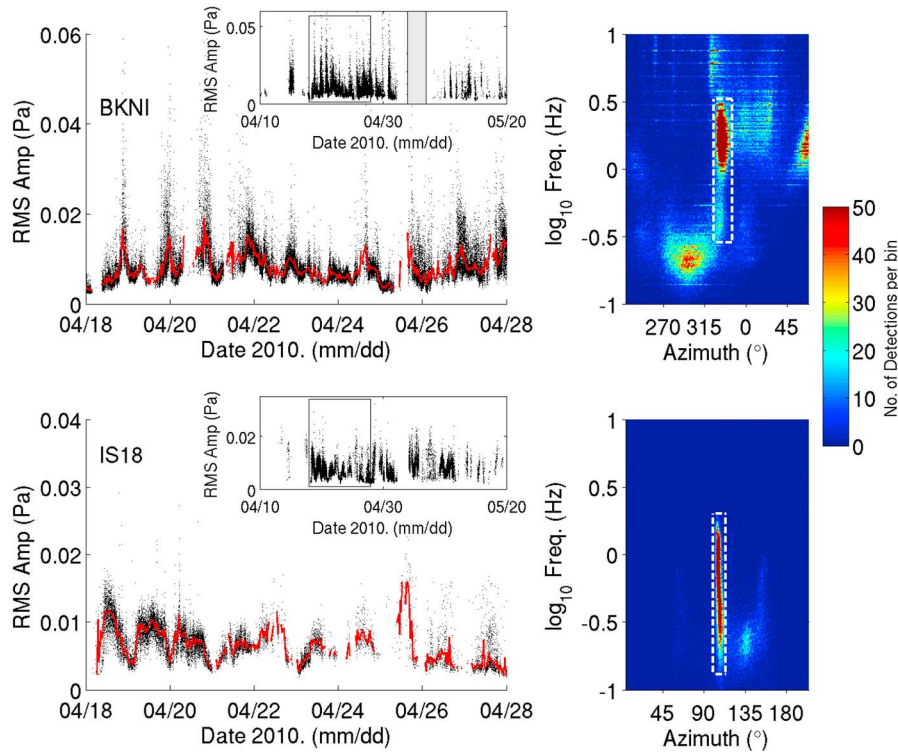
Figure 2. Eyjafjallajökull-associated detections: identification and time series. (top) Results for BKNI. (right) A 2-D histogram of detections in mean frequency-azimuth space over the period 10 April 2010 to 20 May 2010 inclusive. Each frequency-azimuth bin is 1° wide by 0.01 log$_{10}$ (Hz) units tall. The area enclosed within the white dashed line indicates the detections we associate with the Eyjafjallajökull eruption. (left) The larger time series for 10 days of Eyjafjallajökull-associated arrival amplitudes between 18 April 2010 and 28 April 2010, with the median amplitude in 30 min bins provided as a red line. The inset time series shows the extent of the detections across April and May 2010, with the gray shaded area indicating a period of data loss. (bottom) Same as Figure 2 (top) except results for IS18.

aperture of IS18 results in lower intrinsic uncertainties in wavefront parameter estimation. At IS18, for data collected at 20 samples per second, applying the methodology of *Szuberla and Olson* [2004] predicts uncertainties of ~2.5° in azimuth and of ~17 m/s in apparent speed, at the 95% confidence level. In contrast, at BKNI uncertainties are ~4.7° in azimuth and ~27 m/s in apparent speed for data collected at 100 samples per second.

[8] Wavefront parameters for coherent energy propagating across each array were estimated using the PMCC technique [*Cansi*, 1995]. PMCC performs a grid search for coherent acoustic energy in successive time window and frequency band pairs using cross correlation to determine time delays between array elements. Detections within a single time-frequency region (termed a "pixel") are then grouped based on shared wavefront properties. Such groupings have been termed "families," and these groupings define a detection in this paper (for a more in-depth description of the technique, see *Brachet et al.* [2010]). When mean wavefront parameters are reported, these are the mean of the pixel parameter values across a family. Wavefront parameters were also estimated using an F detector scheme, the results of which were in agreement with the PMCC detections. We describe the wavefront velocity vector of each detection by the signal back azimuth, defined as the azimuth from which the detected wave arrived (degrees from North), and the apparent

speed, defined as the wave velocity resolved parallel to Earth's surface in the direction of propagation. All times reported in the paper are given in Universal Time (UT).

[9] Within two-dimensional histograms of detections in back azimuth-frequency space we define rectangular areas for which there are high detection densities, such that any detection within these regions is considered to be associated with the Eyjafjallajökull eruption (Figure 2). For BKNI the signals are contained within the back azimuth range of 325 to 345° and the mean frequency range of 0.28 to 3.3 Hz, whereas at IS18 detections lie within back azimuths of 100 to 114° and frequencies of 0.13 to 2.0 Hz. At both stations the eruption detection population is separated in azimuth from a microbarom detection population centered on approximately 0.2 Hz. The microbarom source is located to the south of Greenland (~40°W, 55°N, Figure 1), a region of known microbarom generation [e.g., *Le Pichon et al.*, 2006].

[10] The detection time series, as shown in Figure 2 and by *Matoza et al.* [2011a], show an onset of signals coincident with the beginning of the Eyjafjallajökull summit eruption on 14 April 2010 [*Gudmundsson et al.*, 2010]. After a cessation of approximately 2.5 days, a high temporal density of infrasound signals are recorded from Eyjafjallajökull at both IS18 and BKNI for the next 10 days (Figures 2 and 3). Eruption infrasound was recorded until approximately 20 May 2010, with the signal waning at BKNI prior to IS18 because of

Table 1. Location of Arrays BKNI and IS18 With Respect to Eyjafjallajökull and Mean and Standard Deviation Values for the Signal Characteristics of the Eyjafjallajökull Eruption Detection Populations Between 18 April 2010 and 28 April 2010

	BKNI	IS18
Range (km)	1745	2286
Azimuth (deg) Source to Station	132.9	331.7
Back azimuth (deg) Stat. to Src.	328.6	104.3
Aperture (m)	210	1170
Number of elements	4	8
Detection back azimuth ($\bar{x}, \sigma$) (deg)	(333.3,3.5)	(106.3,2.5)
Detection V_{app} ($\bar{x}, \sigma$) (km/s)	(0.341,0.014)	(0.340,0.011)
Detection bandwidth (min, max) (Hz)	(0.3,3.3)	(0.1,2.0)

the weakening of the predominant west-to-east stratospheric wind (see section 4).

[11] The signal parameter estimates (amplitude, back azimuth, apparent speed, and mean signal frequency) exhibit a daily periodicity, albeit with differing magnitudes and phase relationships at each station (Figure 3). At BKNI the amplitude and back azimuth estimates appear to vary significantly with a diurnal periodicity: median RMS (root-mean-square) amplitudes calculated across 30 min windows vary between approximately 0.005 and 0.02 Pa, whereas back azimuths vary between approximately 334° and 329° over the daily cycle (Figure 3). At IS18 the diurnal periodicity appears most pronounced for amplitude (between 0.004 and 0.012 Pa), apparent speed (between 0.325 and 0.345 km/s) and mean signal frequency (between 0.25 and 1.2 Hz). In section 3 results of spectral analyses are used to provide robust estimates of the periodicities contained within the signal parameter variations.

[12] The temporal density of detections varies over the day-to-night cycle, with many fewer observations during the daytime period when incoherent pressure fluctuations and wind noise increase at both arrays (see section 3 and Figures 4 and 5). The infrasonic noise amplitude was estimated by calculating a RMS single-channel pressure amplitude in the 0.01 to 0.5 Hz bandpass for 10 min windows, which has been used as a suitable proxy for incoherent wind noise at an array [e.g., *Fee and Garcés*, 2007; *Matoza*
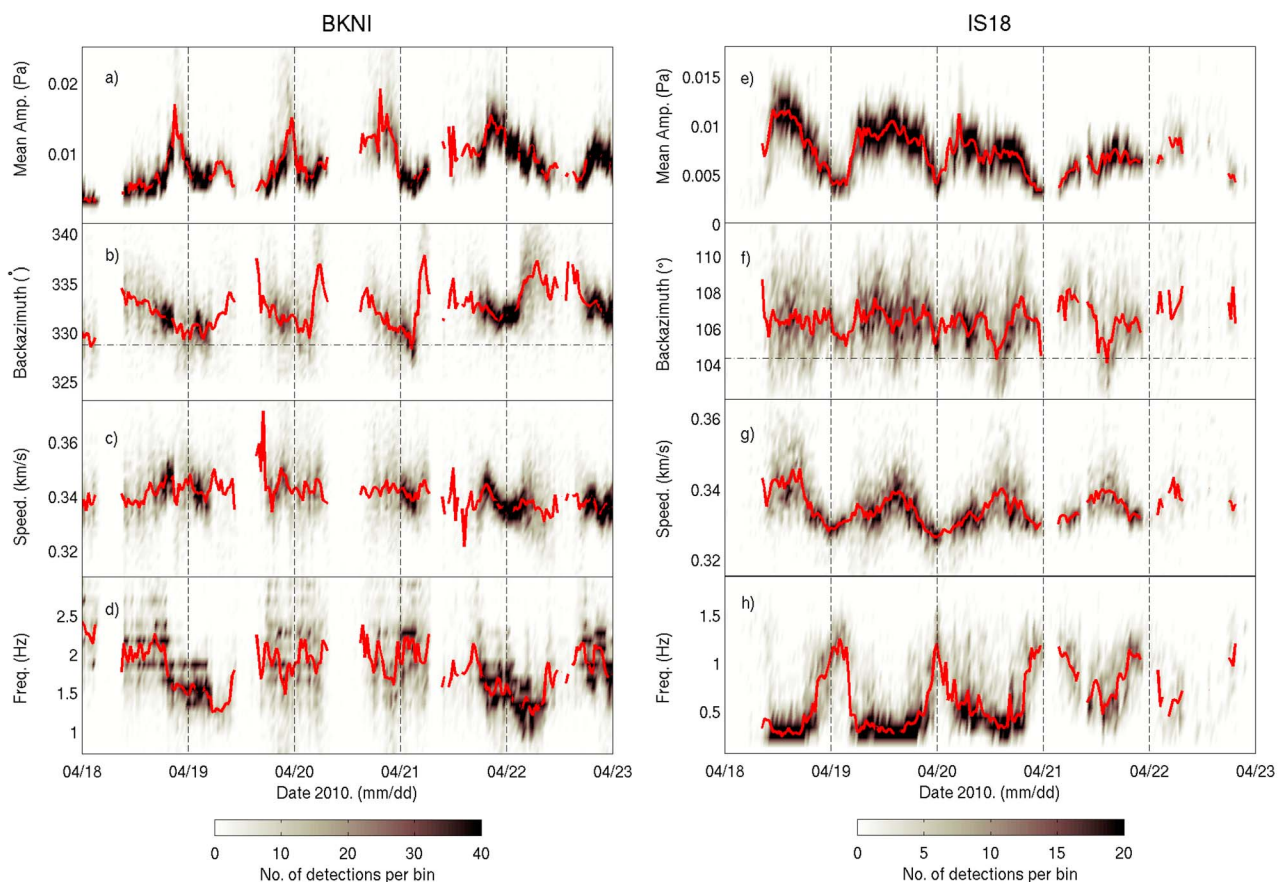

Figure 3. Details of the variations in detection characteristics (mean amplitude, back azimuth, apparent wave speed, and mean frequency) for arrivals at both (a–d) BKNI and (e–h) IS18 for the 5 day period 18 April 2010 to 22 April 2010 inclusive. The shading represents detection density (see color bar) and the red lines represent median values for 30 min nonoverlapping sections. For the density calculations all bins are 30 min long with widths of 0.001 Pa (mean amplitude), 0.5° (back azimuth), 0.002 km/s (apparent speed) and 0.1 Hz (mean frequency). For the back azimuth the horizontal dot-dashed line represents the true receiver-to-source back azimuth.
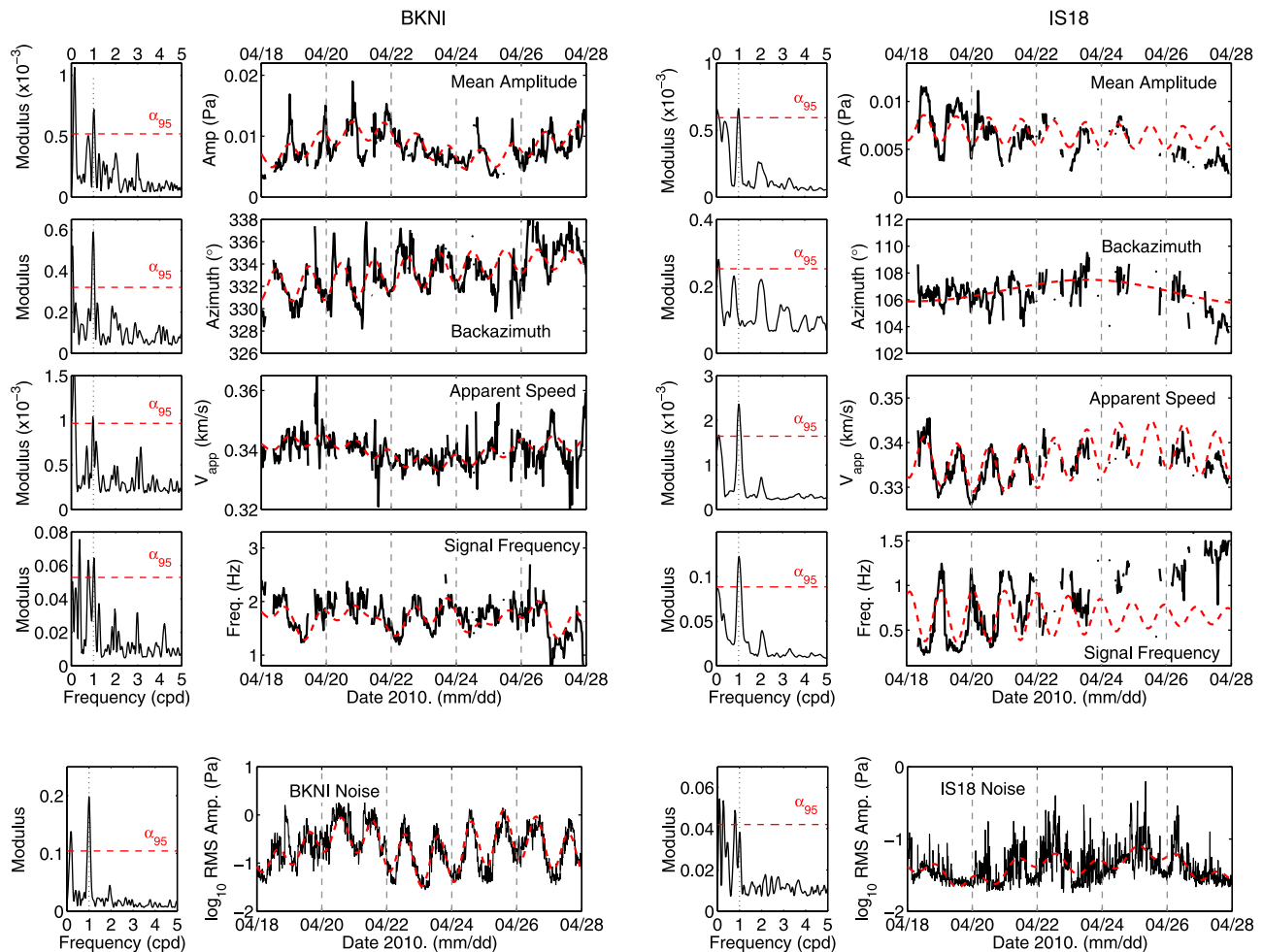
Figure 4. Results of applying the CLEAN algorithm to the detection parameter and $\log_{10}$ RMS noise amplitude time series at both BKNI and IS18 between 18 April 2010 and 28 April 2010. On the power spectra the vertical dotted line indicates the diurnal period (1 cycle per day, cpd) and the α_{95} significance level is shown as a horizontal red dashed line. For the detection parameter time series the black line is the median parameter value calculated for 30 min bins (note the CLEAN algorithm was applied to the raw detection data not the average); for the noise time series the black line is the RMS noise amplitude calculated in the 0.01 to 0.5 Hz bandpass across 10 min windows. The red dashed line is the signal reconstructed from the CLEAN spectra using frequency components whose spectral amplitude value exceeds the α_{95} level.

et al., 2011a]. Reduced detection capability during daytime is expected because solar heating generates increased boundary layer turbulence, increasing incoherent noise and reducing infrasound signal coherency [e.g., *Evers and Haak*, 2005; *Fee and Garcés*, 2007; *Evers and Schweitzer*, 2011]. The diurnal noise fluctuation is most pronounced at BKNI where the noise amplitude decreases by an order of magnitude during the nighttime period (~19:20 and 04:35 UT). The less pronounced fluctuation at IS18 (at a latitude of 77.5°N) may be caused by the 24 h daylight that has just begun in mid-April. In section 3, spectral analyses of wind speed data and meteorological model wind speed predictions are compared with the recorded infrasonic noise amplitude and signal detections. This shows that although diurnal variations in the boundary layer greatly influence the signal detectability, these variations are out of phase with the diurnal signal parameter variations.

[13] A further observation, which is important for the interpretation of diurnal variations, is the negative correlation between signal amplitude and signal mean frequency observed at IS18 (Figure 3). As the mean signal frequency falls the RMS signal amplitude tends to increase. This is a consequence of the mean signal frequency being controlled by the lowest detected frequency within the signal. When the signal contains lower frequencies, or equivalently the signal bandwidth increases, the mean frequency decreases. An increase in signal bandwidth leads to an increased signal amplitude. A full explanation is provided in Appendix A.

3. Spectral Analysis

3.1. Methodology

[14] Spectral techniques for identifying periodicities within a time series typically involve the discrete Fourier
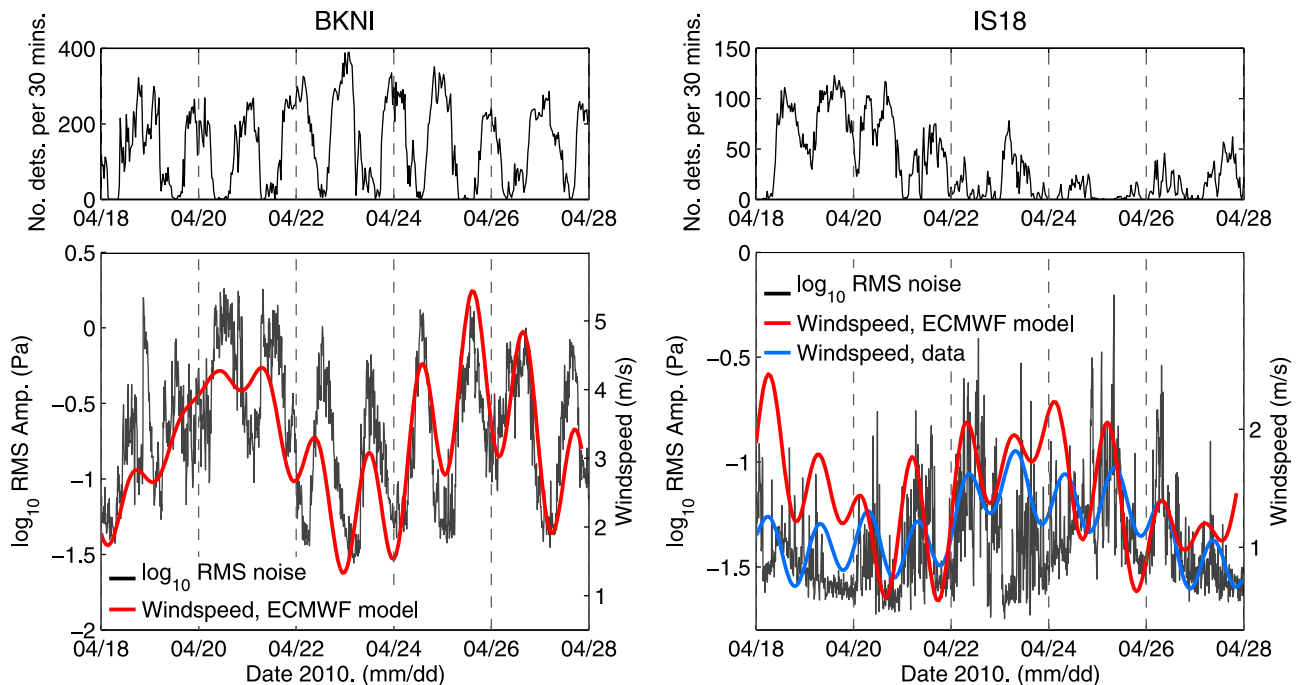
Figure 5. The relationship between (top) the signal detection density and (bottom) the wind-generated noise at both (left) BKNI and (right) IS18. The variations in signal detection density are illustrated using the number of Eyjafjallajökull-associated PMCC detections in consecutive 30 min long bins. In Figure 5 (bottom) the black line is the RMS infrasound noise amplitude calculated in the 0.01 to 0.5 Hz band pass across 10 min windows (see Figure 4). The plotted wind speed magnitudes at the two stations (red lines for ECMWF hindcast model predictions and a blue line for recorded wind speeds at IS18) are the signal reconstructed from the CLEAN spectra using frequency components whose spectral amplitude value exceeds the α_{95} level. All the wind speed time series exhibit a significant diurnal variation.

transform applied to evenly sampled data. However, the time series in this study are unevenly sampled (Figure 3). Techniques have been developed for the analysis of unevenly sampled data series, including the Lomb-Scargle period-ogram [*Press and Rybicki*, 1989] and the CLEAN algorithm [*Roberts et al.*, 1987].

[15] The CLEAN algorithm is used in this paper, primarily because it allows for a simple determination of significance levels for a given spectral peak. The CLEAN method aims to remove the spurious apparent spectral responses that result from the uneven sampling of a time series via an iterative nonlinear deconvolution. Full explanations of the technique as applied to geophysical problems are given by *Baisch and Bokelmann* [1999] (who discuss convergence criteria) and *Heslop and Dekkers* [2002] (who discuss the determination of significance levels via bootstrap methods).

[16] The CLEAN algorithm was applied to signal amplitude, back azimuth, apparent speed, mean signal frequency, and noise amplitude time series recorded at both BKNI and IS18. Different time periods within the detection series were analyzed, and in this paper we present results from the 10 day period between 18 April 2010 and 28 April 2010 (see Figure 2) due to the high density of almost continuous detections (Figure 3). For the same time period the CLEAN algorithm was applied to wind speed data collected at IS18 at a rate of one sample per second (no wind data were collected at BKNI), and meteorological hindcast predictions of wind speed at both stations. The meteorological models

were generated by the European Centre for Medium-Range Weather Forecasts (ECMWF) and provided every 3 h. Wind speeds were taken from the lowest model level (1000 hPa) for comparison with the stations.

[17] We used the method of *Heslop and Dekkers* [2002], and their software can be downloaded from http://www.geo.uu.nl/~forth/Software/soft.html (last accessed March 2012). Each simulation comprised 500 iterations, as suggested by *Heslop and Dekkers* [2002]; during each iteration a tenth of the estimated dirty spectrum, $F_s(\nu)$, was removed. Each simulation calculated the spectrum between 0 and 5 cycles per day, using a random 5% sample of the detections for each of the detection parameters. For the noise measurements a random 10% sample was taken to ensure comparable spectral resolution. For each detection parameter 1000 CLEAN simulations were run, allowing significance levels, α_{95}, to be calculated for the spectral amplitudes. The α_{95} spectral amplitude corresponds to the value exceeded by only 5% of all the spectral amplitudes, across all 1000 simulations. In addition, 95% confidence limits are calculated for the spectral amplitude value estimates at each frequency; these limits show negligible differences with respect to the best estimate of spectral amplitude (approximately equal to the pen thickness on the spectra in Figure 4).

3.2. Results

[18] At BKNI the mean signal amplitude, back azimuth, apparent speed, and mean signal frequency all have significant

Table 2. Details of Which Detection Parameters Have Significant Diurnal Variations at the α_{95} Levels in the CLEAN Analysis[a]

Station	Parameter	α_{95} at Diurnal	Phase (Maximum Hour UT)
BKNI	Mean amplitude	yes	18
	Back azimuth	yes	12
	Apparent speed	yes	22
	Signal frequency	yes	13
	Noise (0.01–0.5 Hz)	yes	14
IS18	Mean amplitude	yes	12
	Back azimuth	no	n/a
	Apparent speed	yes	14
	Signal frequency	yes	0
	Noise (0.01–0.5 Hz)	no	n/a

[a]For those parameters with significant diurnal variations the time at which the diurnal variation maximum occurs is given to the nearest hour. Amplitude is the RMS signal amplitude; frequency is the mean signal frequency; n/a indicates not available.

diurnal variations at the 95% level (Figure 4). The diurnal variations in each detection parameter have varying phase values (see Figure 3 and Table 2), although these values must be interpreted carefully as the parameter variations are not purely sinusoidal (see Figure 3 and spectral harmonics in Figure 4). The most prominent variations are in back azimuth and signal amplitude, with the minimum back azimuth deviations occurring at approximately 01:00 UT, 7 h after the maximum signal amplitudes at 18:00 UT.

[19] At BKNI there are also significant diurnal noise variations, with the maximum noise amplitudes occurring during daytime ($\sim$14:00 UT) when the atmospheric boundary layer is expected to be convecting due to surface heating [e.g., *Garratt*, 1992]. In agreement with previous studies [e.g., *Evers and Schweitzer*, 2011] the noise variations are correlated with significant diurnal oscillations in wind speed at the station, and these variations in noise and boundary layer structure control the signal detectability (Figure 5). However, the variations in noise are not 12 h out of phase with any of the detection parameter variations (Figure 4), as might be expected if the noise amplitudes, or associated boundary layer changes, were controlling the observed diurnal signal parameter variations.

[20] At IS18 significant diurnal variations are observed in amplitude, apparent speed and mean signal frequency but not in back azimuth. The noise also has no significant diurnal variations at the α_{95} level although, again, noise amplitudes are in general elevated during the daytime periods when wind speeds, which do exhibit significant diurnal variations, are highest (Figure 5). The mean amplitude and apparent speed variations are approximately in phase with observed maxima at 12:00 and 14:00 UT, respectively; during times of higher amplitudes the apparent speed of the signals across the array are at a maximum. In addition, the mean signal frequency is at a minimum at times of high amplitude, or equivalently, the signal bandwidth is at a maximum at times of high amplitude (see Appendix A).

[21] To check that these results are robust, the CLEAN algorithm was applied to time series for which the detection parameter values were randomized while the same time sampling was kept. As expected, the results showed no significant diurnal peaks [see *Heslop and Dekkers*, 2002]. In a further check the time series were down sampled such that one random point was retained within each 20 min

portion of the time series. Applying the CLEAN algorithm to these resampled time series reproduced the significant spectral peaks at one cycle per day, providing confidence that the diurnal variations are not an artifact of variable detection density. Also, Lomb-Scargle periodograms generated using the detection data produced results that are extremely similar to those generated by the CLEAN algorithm, providing confidence that the spectral peaks are robust features of the data.

4. Meteorological Models

[22] Acoustic propagation paths through the atmosphere are primarily dependent upon the adiabatic sound speed (c_T) and horizontal wind structure. Both parameters vary with altitude, geographical position and time. In this study the effective sound speed (C_{eff}) is used as an approximation to the combined temperature and horizontal wind speed effect on acoustic propagation, where C_{eff} is defined as

$$C_{eff} = c_T + u_\parallel \tag{1}$$

with $u_\parallel$ being the horizontal wind speed in the direction of propagation, defined as

$$u_\parallel = v\cos\phi + u\sin\phi \tag{2}$$

where v is the meridional wind (positive to the north), u is the zonal wind (positive to the east) and ϕ is the azimuth. The adiabatic sound speed (c_T) is defined as

$$c_T = \sqrt{\gamma_g r T} \tag{3}$$

where $\gamma_g r$, the product of the ratio of specific heats and the gas constant, equals 402.8 $m^2\ s^{-2}\ K^{-1}$ [e.g., *Evers and Haak*, 2010] and T is the absolute temperature (K). One useful parameter that is derived from C_{eff} is Φ_{z_1,z_0}, the ratio of effective sound speed at altitude z_1 and altitude z_0:

$$\Phi_{z_1,z_0} = \frac{C_{eff}(z_1, \text{lon}_1, \text{lat}_1, t_1)}{C_{eff}(z_0, \text{lon}_0, \text{lat}_0, t_0)} \tag{4}$$

where $C_{eff}(z_0, \text{lon}_0, \text{lat}_0, t_0)$ is the effective sound speed determined at the source location ($z_0, \text{lon}_0, \text{lat}_0$) and origin time ($t_0$), while $C_{eff}(z_1, \text{lon}_1, \text{lat}_1, t_1)$ is calculated at locations and times along the raypath. Φ_{z_1,z_0} provides an indication of whether, in the geometrical acoustics approximation, refraction back toward the source altitude, z_0, is expected. If Φ_{z_1,z_0} becomes larger than 1 for upward traveling acoustic energy, then refraction is expected back toward the source altitude. For both the Eyjafjallajökull to BKNI and Eyjafjallajökull to IS18 paths the lower altitude is taken to be the source altitude ($z_0 = 1.5$ km asl, the volcano summit). The upper altitude is taken as the mean altitude of maximum C_{eff} in the stratosphere. For the Eyjafjallajökull to BKNI path this is 50 km (so $\Phi_{50,1.5}$ is used) and for the Eyjafjallajökull to IS18 path this is 52 km (so $\Phi_{52,1.5}$ is used). For discussions of back azimuth deviations, the crosswind, $u_\perp$, is defined as being positive in the direction 90° clockwise from the direction of propagation.

[23] The atmospheric specifications of temperature and wind speed used in this paper are derived from numerical
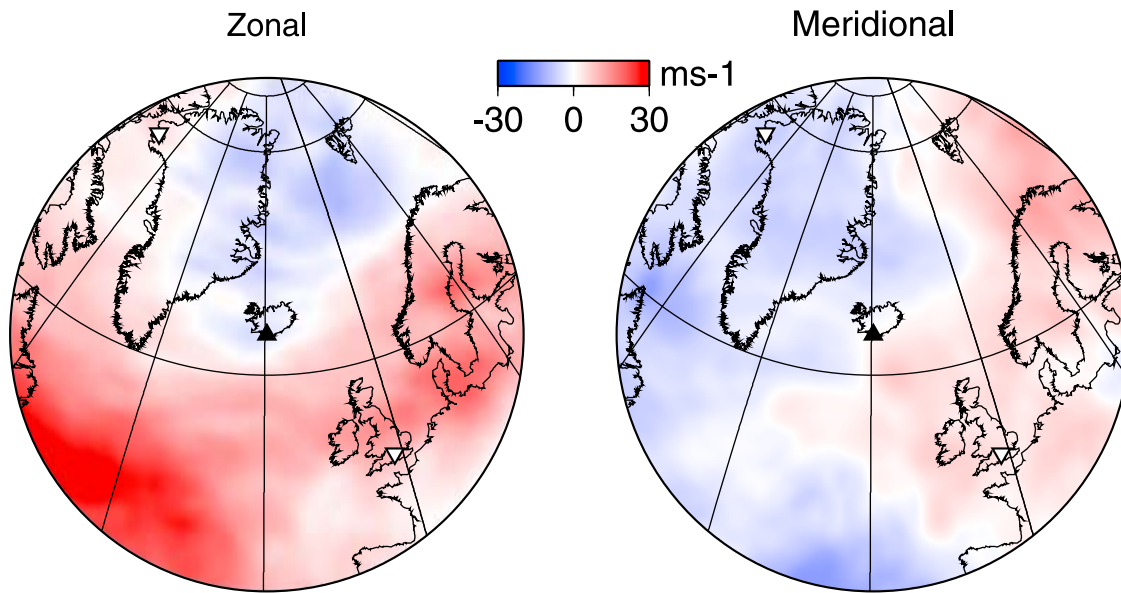
Figure 6. The ECMWF zonal wind (positive values indicate flow to the east) and meridional wind (positive values indicate flow to the north) fields at an altitude of 50 km at 00:00 UT 23 April 2010. Eyjafjallajökull is depicted by the black triangle, whereas the two stations (BKNI, UK, and IS18, Greenland) are given as inverted white triangles. The map is an azimuthal equidistant projection, for which distances and bearings from the center point (Eyjafjallajökull) remain true.

weather (hindcast) predictions of the ECMWF. These models consist of 91 levels from 1000 to 0.01 hPa (approximately an altitude range of 0 to 80 km) and are provided every 3 h. To incorporate the upper mesosphere and lower thermosphere, the ECMWF profiles are fused with the climatological models MSIS90 [*Hedin*, 1991] and HWM07 [*Drob et al.*, 2008], increasing the altitude range to 180 km.

[24] During April 2010 the eastward wintertime stratospheric zonal flow was weakening prior to the switch to summertime westward flow; therefore, westward zonal flow occurred close to the stratopause to the north of Eyjafjallajökull, while to the south of Iceland eastward zonal flow dominated (Figure 6). These conditions allowed stratospheric acoustic ducts to form along both the Eyjafjallajökull to BKNI and Eyjafjallajökull to IS18 propagation paths (e.g., Figures 7 and 8). The synoptic conditions also show the spatial variability of the stratospheric winds along the acoustic propagation paths; for the Eyjafjallajökull to BKNI propagation path there is pronounced strengthening of the wind amplitudes toward Europe (Figure 6). This along-path variability has implications for the ducting of infrasound along the path, as detailed in section 5.

[25] Also of importance to the acoustic propagation is the presence of a strong tropospheric acoustic duct along the Eyjafjallajökull to BKNI path (Figure 7). This lower atmospheric duct is generated by wind flows directed to the south and southeast associated with an anticyclone located to the south of Iceland [*Petersen*, 2010]. The top of the duct is generated by along-path winds of between 20 and 40 m/s at an altitude of approximately 10 km. No such tropospheric acoustic duct is present along the Eyjafjallajökull to IS18 path due to acoustic propagation against the mean flow.

[26] In addition to spatial variations, temporal variations in the acoustic ducting are also apparent within the meteorological models. Figures 7 to 9 show clear diurnal variations

in stratospheric C_{eff} along both the Eyjafjallajökull to BKNI and Eyjafjallajökull to IS18 paths. These stratospheric variations are primarily driven by changes in wind speed rather than temperature: ~15 to 20 m/s change in along-path wind speeds (Figure 10a) compared to ≤7°C change in temperature (corresponding to ≤4 m/s change in sound speed) over the diurnal cycle. These wind speed changes are of high-amplitude compared to the those typically expected (5 to 15 m/s) for stratospheric tides [*Forbes and Groves*, 1990]. For the Eyjafjallajökull to BKNI path the strongest acoustic ducts occur between 21:00 and 00:00 UT, while for the Eyjafjallajökull to IS18 path the strongest acoustic ducts occur between 15:00 and 18:00 UT. This phase shift in duct strength between the two stations is a function of the difference in propagation path direction, the geographical position of the paths and the migration of the Sun's illumination of Earth's surface.

[27] For the tropospheric duct, although there is temporal variability in the amplitude of the along-path effective sound speed, there is no pronounced diurnal variation (Figure 10b). Although there is meteorological evidence for a diurnal variation in volcanic plume height, associated with a shallow nighttime capping inversion at altitudes of 2.2–2.6 km [*Petersen et al.*, 2012], this inversion is not resolved in the ECMWF models. However, the amplitudes of the diurnal changes in temperature (<4°C) suggest that this inversion would have a negligible influence on acoustic ducting.

5. Propagation Modeling

[28] In this study, numerical modeling is undertaken in order to gain an understanding of how diurnal atmospheric variability may modify the propagation paths, and consequently vary the observed signal parameters. The modeling was conducted using the 3-D Hamiltonian acoustic ray-tracing
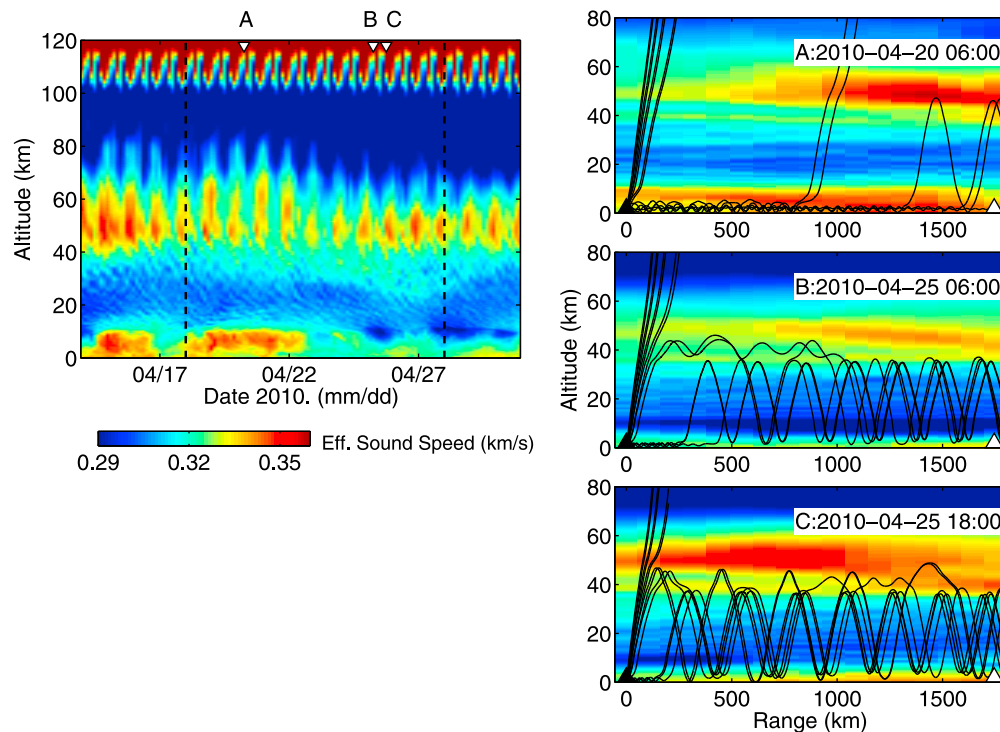
Figure 7. The time and range dependence of the effective sound speed ($C_{eff}(z)$) for the Eyjafjallajökull to BKNI path. (left) Temporal changes in $C_{eff}(z)$ above Eyjafjallajökull for the period 14 April 2010 to 30 April 2010 inclusive. The black dashed lines delimit the time for which the CLEAN spectral analyses were conducted (Figure 4). (right) The range dependence of $C_{eff}(z)$ along the Eyjafjallajökull (black triangle) to BKNI (white triangle) path for three specific times: A, 06:00 UT 20 April 2010; B, 06:00 UT 25 April 2010; and C, 18:00 UT 25 April 2010. Rays shot through the interpolated 3-D meteorological model for takeoff angles at 10° intervals between 60° and 120° from the vertical have been included to indicate dominant acoustic paths. No returns from the thermosphere are shown to ensure figure clarity; all such returns are attenuated by >180 dB at source-to-station ranges.

code, WASP-3D [*Dessa et al.*, 2005; *Virieux et al.*, 2004]. This technique accounts for the effects of spatial and temporal variations in the temperature and horizontal wind structure on the acoustic propagation paths. Ray-tracing simulations along both paths (Eyjafjallajökull to BKNI and IS18) were performed using the 3-hourly ECMWF meteorological specifications over the period 14 April 2010 to 28 April 2010 inclusive. Rays were shot from the source toward the receiver within an angular swath between 60 and 120° from the vertical at 1° intervals. The source height was kept constant at 1.5 km above sea level. This altitude corresponds to the volcano summit, as we consider the infrasound source to be located at, or close to, the vent. *Matoza et al.* [2011b] showed the importance of accounting for the source altitude; the meteorological conditions at the vent have an influence on the resultant propagation.

[29] The model also allows for the calculation of amplitudes, via paraxial rays, and takes into account geometrical spreading and intrinsic attenuation [*Sutherland and Bass*, 2004]. In this study the amplitude values are only used to remove rays from the analysis that experience an amplitude drop of >180 dB along the propagation path, and would therefore not be observed at the recording stations.

[30] The simulations in this paper use range-dependent meteorological specifications, but the specifications do not change during the propagation duration; that is, the

specifications at all ranges are taken at the same time. This is justified as the temporal resolution of the specifications (3 hourly) is less than the source-to-receiver propagation times (∼1.6 h to BKNI, ∼2.1 h to IS18).

[31] To simplify the modeling, and to allow us to isolate the effects of meteorology, the simulations do not include surface topography. Models of infrasound interaction which include terrain have shown enhanced scattering of acoustic energy within preexisting atmospheric waveguides [e.g., *Arrowsmith et al.*, 2007]. In this study, the effect of topography along the Eyjafjallajökull to BKNI path is expected to be minimal; much of the path is across the ocean. The effect of topography along the Eyjafjallajökull to IS18 path is potentially more significant as a large proportion of the propagation path is across the Greenland ice shelf (Figure 1). However, the addition of topography would be a time-independent correction, and hence will not significantly influence the temporal variations investigated in this paper.

[32] Because our ray-tracing simulations were conducted at 1° intervals in takeoff angle, the simulations only sample a fraction of the acoustic wavefield. Therefore, to identify observable acoustic returns at a station on Earth's surface, we follow *Matoza et al.* [2011b] and consider rays to arrive at the station if they reach the ground within ±50 km of the receiver. This area is chosen empirically to ensure that rays are considered to arrive at the station when the wavefield
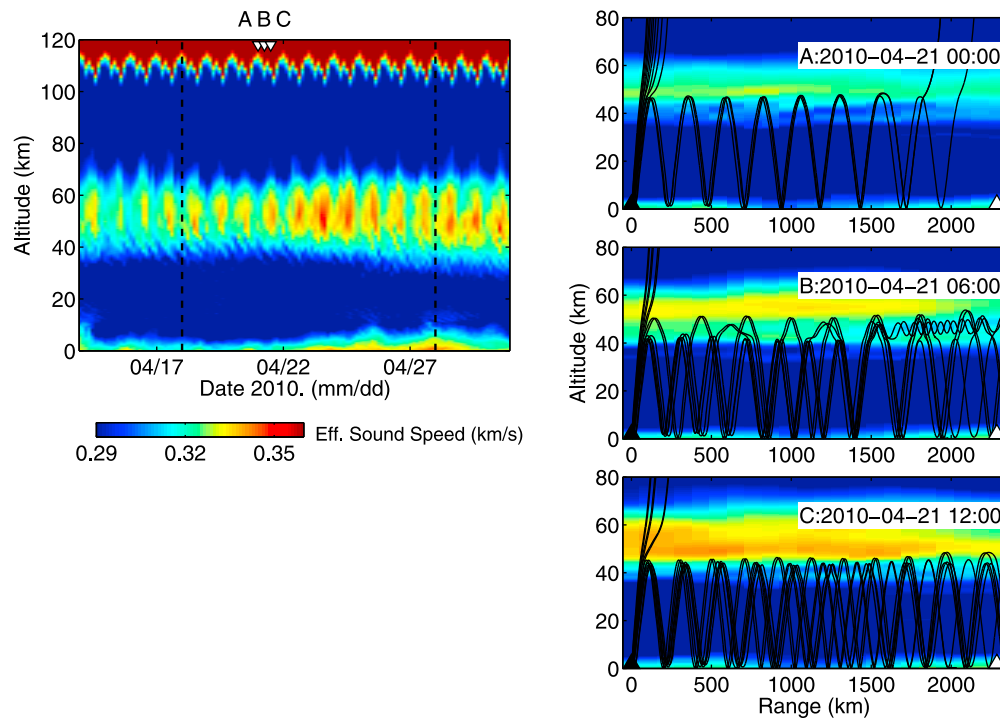
Figure 8. Same as Figure 7 except for the Eyjafjallajökull to IS18 path. The three specific times for which ray tracing solutions are shown are A, 00:00 UT 21 April 2010; B, 06:00 UT 21 April 2010; and C, 12:00 UT 21 April 2010.
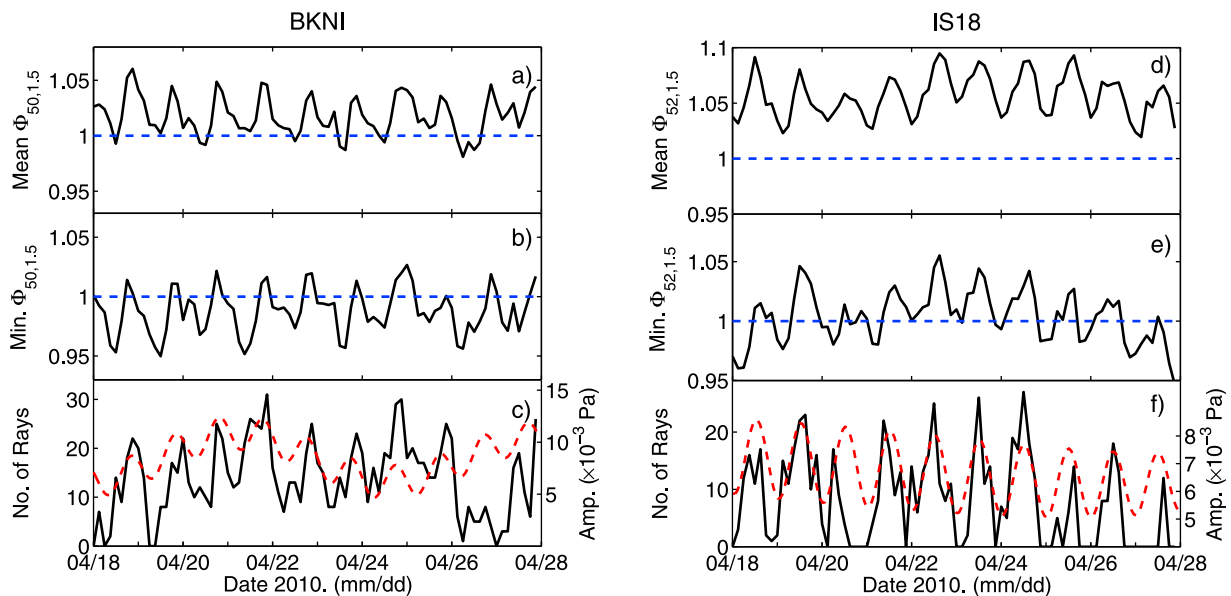

Figure 9. A comparison of (a) the ratios of the mean along-path effective sound speed at altitudes of 50 and 1.5 km ($\Phi_{50,1.5}$) and (b) the minimum along-path effective sound speed ratio ($\Phi_{50,1.5}$) with (c) the number of rays that land within ±50 km of BKNI in the propagation models (Figure 8). The altitude of maximum effective sound speed is 50 km; the source altitude is 1.5 km. The blue dashed line corresponds to an effective sound speed ratio equal to 1. Figure 9c also includes as a red dashed line the significant observed amplitude variations as identified using the CLEAN algorithm (Figure 4). (d–f) Illustration of the values for the Eyjafjallajökull to IS18 path. Note that for this path the approximate altitude of maximum effective sound speed is 52 km.
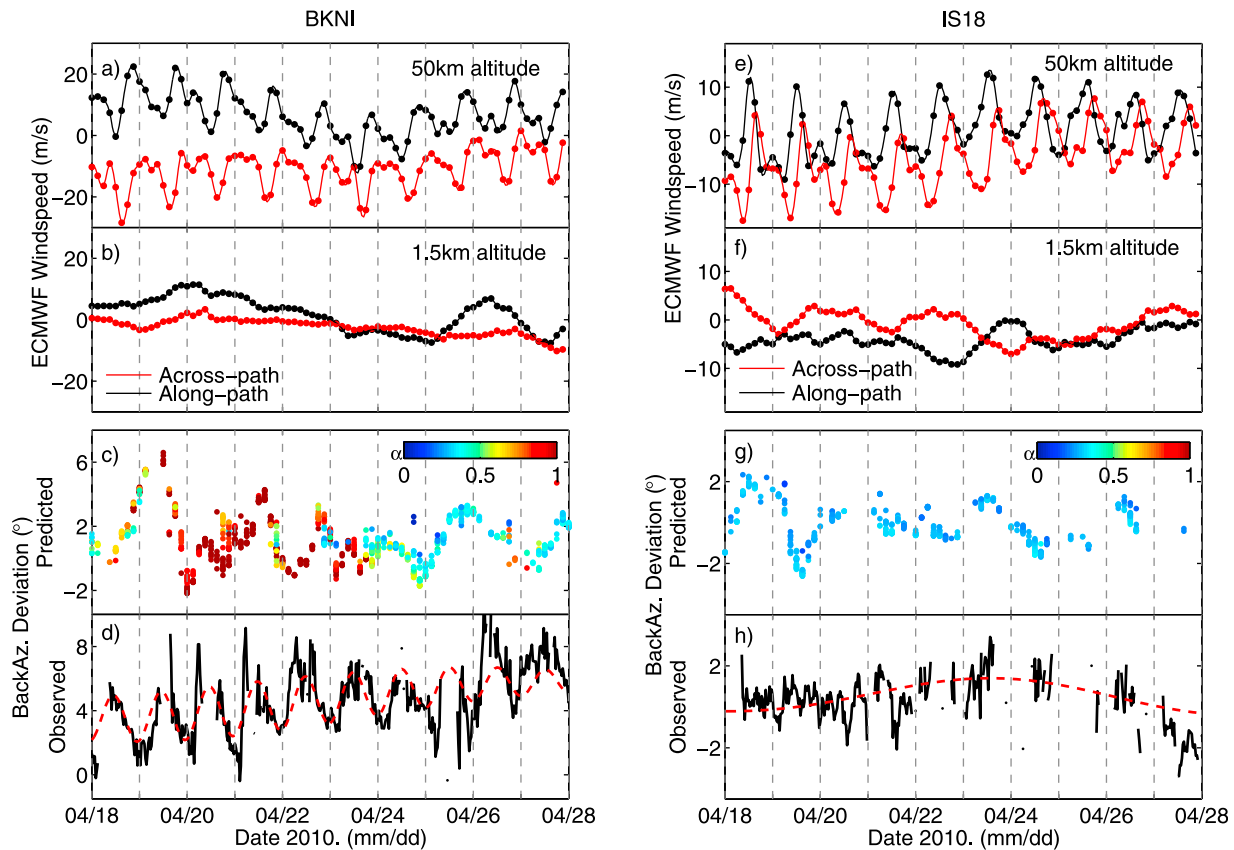
Figure 10. Variations in ECMWF wind speeds, compared to predicted and observed back azimuth deviations. (a) The mean temporal wind speed variations along path (black) and across path (red) at an altitude of 50 km for the Eyjafjallajökull to BKNI path. The dots show the times at which meteorological specifications are available; the lines are cubic spline interpolations between these points. (b) The along- and across-path wind speeds at the source altitude (1.5 km) on the same scale as Figure 10a. (c) The modeled back azimuth deviation (predicted - true) for rays arriving within ±50 km of BKNI. The individual predictions are colored according to α, the proportion of the raypath length located at altitudes less than 15 km. (d) The observed back azimuth deviation (black lines) and the signal reconstructed from the CLEAN spectra (red lines; see Figure 4). (e–h) Same as Figures 10a–10d except for the Eyjafjallajökull to IS18 path; the observed back azimuths in Figure 10h have been corrected for the effect of the IS18 interelement altitude differences (see text).

impinges near the receiver, but arrivals from returns unlikely to be observed are excluded.

[33] In the context of the Eyjafjallajökull observations it is important to recognize that ray tracing is a high-frequency approximation to the full acoustic wavefield. Therefore, the results of ray tracing do not account for effects such as diffraction and scattering which can play a large role in returning acoustic energy to Earth's surface [e.g., *Kulichkov et al.*, 2010; *Green et al.*, 2011]. Nevertheless, the results of ray tracing provide insight into which acoustic propagation paths are present during the Eyjafjallajökull eruption period. Figures 7 and 8 provide three examples of the ray-tracing results between Eyjafjallajökull and both BKNI and IS18, showing the different acoustic propagation paths between the source and receivers.

[34] In an attempt to model any finite frequency effects a 1-D parabolic equation code was run using mean along-path sound speed profiles. However, as described further in section 5.2, this was unsuccessful due to the importance of including range dependence.

[35] As with all global infrasound studies, the propagation modeling results will be influenced by the resolution of the meteorological specifications used. In this study we do not include the effects of gravity waves or wind shear that have been shown to have significant influence on infrasound propagation in some studies [e.g., *Kulichkov*, 2004; *Green et al.*, 2011]. However, the primary purpose of the propagation modeling presented here is not to accurately replicate the observed signal waveform amplitudes or durations, but to ascertain whether tides resolved in the meteorological specifications can assist in interpreting the Eyjafjallajökull observations.

5.1. Eyjafjallajökull to BKNI

[36] Along the Eyjafjallajökull to BKNI path (Figure 7), the spatiotemporal variations in meteorological structure control which rays propagate to the station. Between 18 April 2010 and 28 April 2010 the stratospheric duct is weak close to the source, strengthening toward the station (Figures 6 and 7). Therefore, energy that travels up into the stratosphere

directly from the source is often not returned to the ground; for 28% of the 10 day period $\Phi_{50,1.5}$ directly above Eyjafjallajökull is less than 1. In addition, a pronounced tropospheric duct is present along the path (Figure 7). The tropospheric duct velocity minimum is at an altitude of ~2 km, close to the acoustic source altitude. Therefore, the simulations predict that significant numbers of rays are trapped in a narrow altitude range around the velocity minimum of the tropospheric duct, either over the whole path (time period A, Figure 7) or within the first few hundred kilometers of the path prior to leaking into a stratospheric duct (time periods A, B and C, Figure 7).

[37] Although tropospheric infrasound propagation has been observed up to ranges of a few hundred kilometers [e.g., *Hagerty et al.*, 2002; *Negraru and Herrin*, 2009], the authors know of no reported tropospheric propagation out to ranges of ~2000 km. Therefore, any modeling results which rely heavily on long-range (>500 km) tropospheric propagation will be treated with scepticism. However, as shown in time period B of Figure 7, ray-tracing modeling predicts that tropospheric ducting close to the source is required to enable acoustic energy propagation between Eyjafjallajökull and BKNI.

[38] Within the simulations for the 18 April 2010 to 28 April 2010 time period 21% of all simulated raypaths were returned to within ±50 km of BKNI and only 22% of these rays propagated exclusively within a stratospheric duct (32% propagated exclusively within a tropospheric duct while the remaining 46% propagated within both tropospheric and stratospheric ducts along the propagation path).

[39] Within the meteorological specifications, diurnal variations are only present at stratospheric altitudes and above (Figures 7, 10a, and 10b). In the simulations a significant diurnal variation at the α_{95} level is predicted in the number of rays arriving within ±50 km of BKNI (Figure 9c). This diurnal variation is a consequence of rays with takeoff angles between 5 and 15° away from the horizontal only being trapped within the stratospheric duct during times of higher C_{eff} at the stratopause (Figure 7, time period C). Rays with takeoff angles closer to the horizontal tend to be preferentially trapped in the shallow tropospheric duct.

[40] The variations in simulated back azimuth are strongly influenced by the high proportion of acoustic propagation within the shallow tropospheric duct. The back azimuth variations are controlled by a combination of time-dependent changes in the length of the propagation within the tropospheric duct, the strength of the tropospheric crosswinds, and the along-path structure of the tropospheric crosswinds. These variations depend upon the meteorology, but are not controlled by tidal variations (Figures 7 and 10b). Therefore, although the observed back azimuths exhibit significant diurnal variations, none are predicted by the simulations (Figures 10c and 10d).

5.2. Eyjafjallajökull to IS18

[41] The results of the simulated propagation between Eyjafjallajökull and IS18 predict that 99% of the rays returned to within ±50 km of IS18 propagate exclusively within a stratospheric duct (Figure 8). The remaining 1% have a fraction of the raypath within a tropospheric duct (and in 80% of these cases the tropospheric raypath is less than 200 km in length).

[42] Diurnal variations in stratospheric effective sound speed (Figure 8) result in diurnal variations in the numbers of returned rays; these variations are significant at the CLEAN α_{95} level. Between 18 April 2010 and 28 April 2010 the number of rays propagating to within ±50 km of IS18 at 12:00 UT is, on average, six times greater than the number at 00:00 UT (Figure 9f). This is the result of a wider range of ray takeoff angles returning energy to the ground at times of higher C_{eff}. Rays from the 1.5 km altitude source are returned to the sensors with takeoff angles between 74° and 108° from the upward vertical at the C_{eff} maximum (~12:00 UT) compared to between 82° and 96° at the C_{eff} minimum (~00:00 UT). The rays having takeoff angles between 80° and 100° from the upward vertical (i.e., greater than 10° away from the horizontal) are only ducted when the effective sound speed in the stratosphere is >5% larger than that at the source (i.e., $\Phi_{52,1.5} > 1.05$).

[43] The mean predicted back azimuth deviations at IS18 are in agreement with the observations (Figures 10g and 10h). During the 18 April 2010 to 28 April 2010 period the mean observed back azimuth deviation, predicted value minus true value, is 1.8° ± 1.3° (mean ± one standard deviation). However, as shown by *Edwards and Green* [2012], these values must be corrected for the effect of significant interelement topography at IS18. For a plane wave arriving from Eyjafjallajökull, and an incidence angle consistent with a stratospheric arrival (75° from vertical), the correction at IS18 is −1.8°. Therefore, the corrected observed values are 0.0° ± 1.3° compared to the predicted values of −0.2° ± 1.0°.

[44] No significant diurnal variations in back azimuth variations are predicted (Figure 10g), consistent with the absence of observed diurnal variations (Figure 4). Two causes contribute to the lack of predicted back azimuth diurnal variations. First, the tidal components of the crosswind (Figure 10e) do not have a significant influence because they are restricted to altitudes of 45 km and higher (e.g., Figure 8), which is <10% of the raypath length. Second, the back azimuth variations are controlled by the integral of the crosswind along the propagation path. For the Eyjafjallajökull to IS18 path the maximum crosswind amplitudes throughout the troposphere and lower stratosphere (<35 km altitude) have a median value that is 90% of the maximum close to the stratopause. Therefore, on this path, the troposphere and lower stratospheric crosswinds have a large influence on the back azimuths.

[45] The changes in effective sound speed with time also provide a clear illustration of the range-dependent nature of the acoustic duct between Eyjafjallajökull and IS18. The mean effective sound speed ratios ($\Phi_{52,1.5}$) along the path are always greater than one (Figure 9d); if this was true along the entire path length, it would be expected that acoustic energy was always ducted between 18 April 2010 and 28 April 2010. However, the minimum along-path effective sound speed ratio oscillates around a value of one with a diurnal period (Figure 9e). In the high-frequency ray theory approximation this is consistent with a diurnal oscillation between stratospheric acoustic ducting ($\Phi_{52,1.5} > 1$ along entire path) and time periods where refraction near the stratopause is not expected along some portion of the propagation path (minimum $\Phi_{52,1.5} < 1$). At locations and times where $\Phi_{52,1.5} < 1$ acoustic energy will leak upward into the thermosphere.
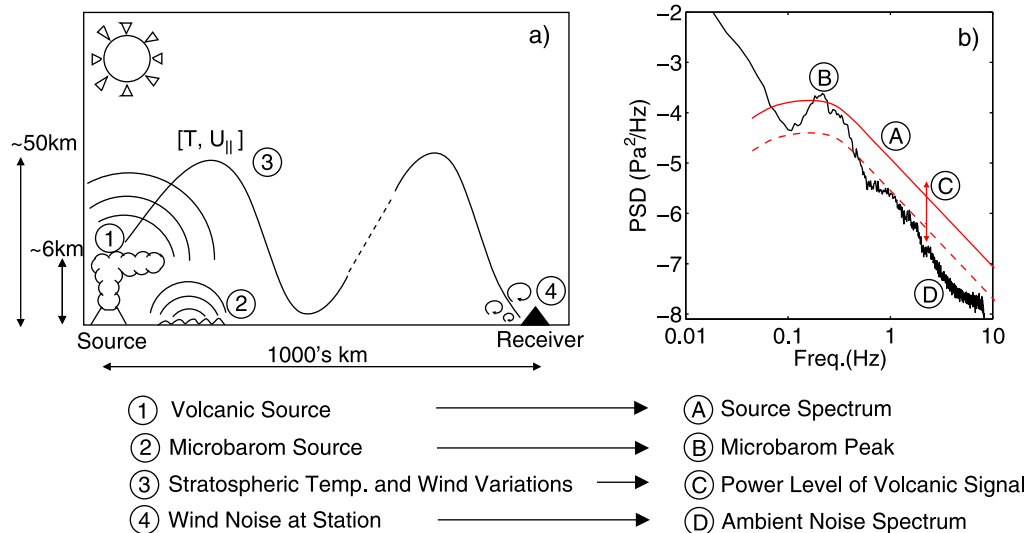
Figure 11. A cartoon showing (a) the major sources of infrasound and ambient noise alongside the factors influencing propagation for the Eyjafjallajökull to IS18 path and (b) the effect on the recorded spectral information. It is expected that the influence of the solar tide will cause the temperature (T) and along-path wind speeds ($U_{\parallel}$) close to the stratopause altitude to vary on diurnal timescales. This will have a corresponding effect on the signal-to-noise ratio and the observable bandwidth of the signal; the recorded signal power is expected to be higher when propagation within the stratospheric duct is more efficient.

Once energy is lost from the stratospheric duct it is expected that this portion of the wavefield will not be returned to IS18, due to the high acoustic attenuation in the thermosphere.

[46] The importance of including range dependence explains why 1-D parabolic equation (PE) simulations did not predict a diurnal signal amplitude variation at IS18. This modeling was conducted using a linear wide-angle PE code [*Collins*, 1993] with a range-independent velocity model constructed from the mean along-path effective sound speed profiles. The PE simulations calculated acoustic transmission losses along the propagation path every 4 h between 00:00 UT, 18 April 2010 and 21:00 UT, 28 April 2010 at frequencies of 0.02, 0.08, 0.32, and 1.28 Hz. No periodic variations in simulated transmission loss were observed at any frequency. This was a consequence of using mean along-path effective sound speed profiles. As little energy was lost from the stratospheric duct ($\Phi_{52,1.5} > 1$ at all times; Figure 9d) the simulated amount of energy being propagated within the stratospheric duct remained approximately equal at all times, regardless of the diurnal cycle.

6. Interpretation of Results

[47] The numerical propagation modeling results are used to assist the interpretation of the observed diurnal infrasound wavefront parameter variations. The cause of the variations is assessed, in particular whether it is possible to separate any source, propagation and receiver effects (Figure 11).

6.1. Eyjafjallajökull to IS18

[48] Along the Eyjafjallajökull to IS18 path significant diurnal variations were observed in amplitude, signal bandwidth and apparent speed (Figure 4). All three of these signal parameters exhibited diurnal maxima at approximately 12:00 UT (Figure 12) with the variations in amplitude and

signal bandwidth being closely related (Appendix A). The increase in bandwidth is interpreted as being the result of increased observed signal power due to propagation through a more efficient stratospheric acoustic duct. This efficient duct is identified by higher $\Phi_{52,1.5}$ values, and increased numbers of simulated rays reaching the station in phase with the observed diurnal amplitude variations (Figure 9f). The increased signal power, and hence signal-to-noise ratio (SNR), at ~12:00 UT is of largest consequence within the 0.07 to 0.4 Hz frequency band where the increased SNR allows the Eyjafjallajökull signal to be detected above the microbarom peak (see solid red line in Figure 11b and Appendix A for the data). Detection in this frequency band is not possible at the diurnal minima (00:00 UT) because of the decreased SNR (dashed red line, Figure 11b). The interpretation that a more efficient stratospheric duct generated the amplitude, and hence bandwidth, variations is also consistent with the observed diurnal variation in apparent speed (Figures 4 and 12). At times of more efficient acoustic ducting (high $\Phi_{52,1.5}$ values), acoustic energy with an increased takeoff angle with respect to the horizontal will be refracted back to Earth's surface from the stratosphere (Figure 8). As energy with higher takeoff angles is ducted, the mean apparent signal speed across IS18 increases as a consequence of steeper wavefronts passing across the array. The lack of an observed diurnal variation in back azimuth is also consistent with the numerical modeling results, where any diurnal variations are masked by larger amplitude fluctuations resulting from changeable tropospheric and lower stratospheric crosswind amplitudes (Figure 10 and section 5.2).

[49] Although a stratospheric acoustic duct undergoing diurnal variations in strength (e.g., Figure 8) can qualitatively explain the observed diurnal parameter variations, an alternative explanation to consider is whether changes at
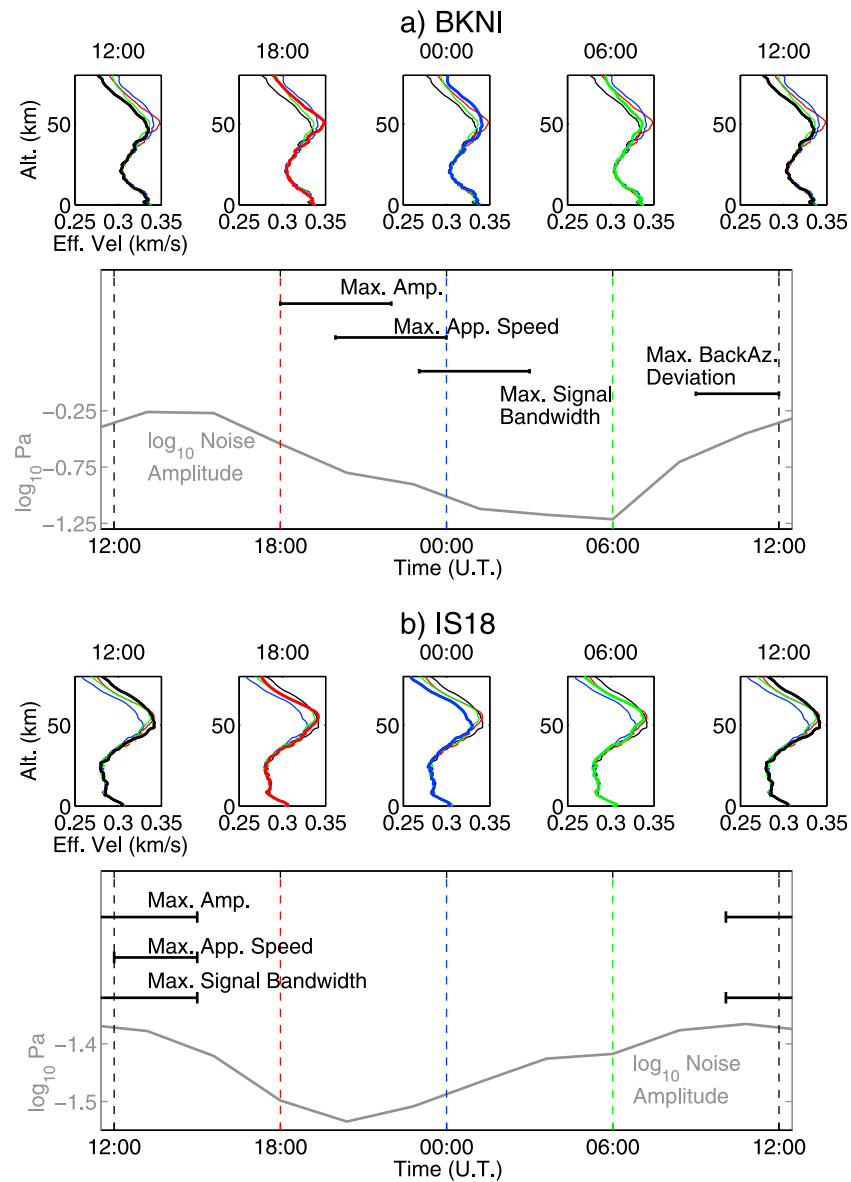
Figure 12. The temporal relationships between the variable stratospheric ducts, the signal parameter variations and the noise amplitudes at both (a) BKNI and (b) IS18. The along-path effective sound speed profiles illustrate the median effective sound speed profile at the midpoint of the volcano to station propagation path at the given time over the period 18 April 2010 to 28 April 2010. The profile at each time is identified by a specific color. The noise amplitudes are median values, in the 0.01 to 0.5 Hz band pass, across 2.5 h windows for the same period. The time ranges for the signal parameter maxima are provided as indicators of when the maxima are observed, consistent with the results of the CLEAN spectral analyses.

the source or the receiver generate similarly plausible interpretations.

[50] If the explosive emissions of Eyjafjallajökull were diurnally modulated, the changes in SNR might be explained by a varying source term. Although variations of some, usually low-amplitude, volcanic activity has been shown to exhibit diurnal modulation [e.g., *Neuberg*, 2000] such a model would be unable to explain the observed diurnal changes in apparent signal speed at IS18. In addition, M. Ripepe kindly provided us with data from an infrasound array, ICLND, deployed approximately 9 km from the summit

vents at Eyjafjallajökull in rapid response to the volcanic crisis of April and May 2010. Good quality data are available from 13 May 2010, and the CLEAN algorithm has been applied from then to 25 May 2010; no significant diurnal variations are observed in any parameter at the α_{95} level. Although this is consistent with the hypothesis that there was no strong diurnal variation at the source, no ICLND data are available between 18 April 2010 to 28 April 2010 when significant observations of diurnal variations were made at BKNI and IS18.
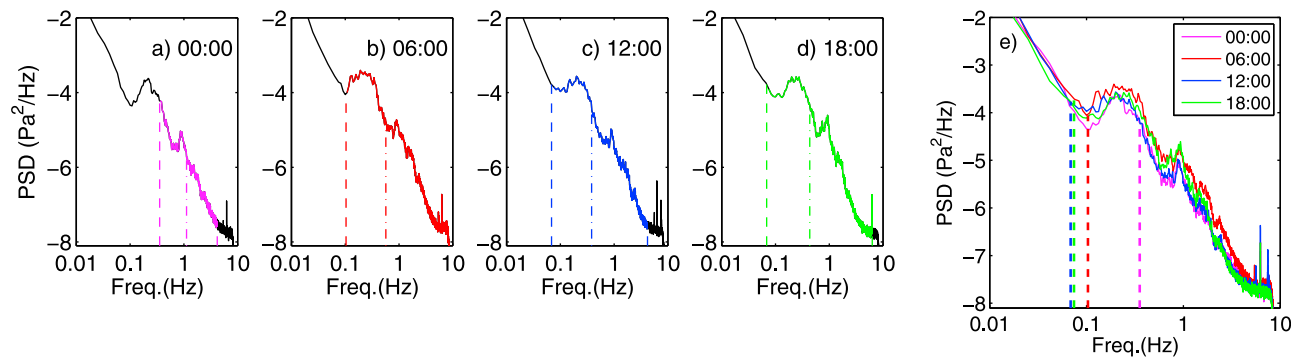
Figure 13. Power spectral density (PSD) estimates of IS18 beam-formed data for hour long segments on 20 April 2010 (the times given are the start of each segment). The beams are generated using the mean azimuth and apparent speed parameters from volcanic signals recorded during each hour. (a–d) Individual hour PSD estimates with the colored sections indicating the frequency range of detections associated with Eyjafjallajökull. The vertical dashed lines indicate the lower and upper limits of the signal bandwidth, and the vertical dot-dashed lines indicate the mean signal frequency. (e) An overlay of the four PSD estimates, with the vertical dashed line indicating the minimum signal frequency for each hour.

[51] Strongly diurnally varying noise at a receiver, ~12 h out of phase with the signal amplitude variations, would lead to signals being preferentially recorded at times of low noise and an increase in the observable signal bandwidth with decreasing noise (increasing SNR). This is not observed at IS18 (Figure 4); indeed maximum observed noise levels are at times of maximum signal amplitude (Figures 12 and 13). A diurnally varying receiver effect is also unable to account for the diurnal apparent speed variations. Therefore, although diurnally varying noise at the receiver controls the signal detectability (Figure 5), the preferred mechanism to explain diurnal infrasound parameter variations along the Eyjafjallajökull to IS18 path are effective sound speed changes close to the stratopause, i.e., stratospheric solar tides.

6.2. Eyjafjallajökull to BKNI

[52] Along the Eyjafjallajökull to BKNI path significant diurnal variations are observed in signal amplitude, back azimuth, apparent speed, and mean frequency (Figure 4). In addition, the noise at BKNI also varies diurnally.

[53] The diurnal variations in amplitude and apparent speed can be explained using the same arguments as for the Eyjafjallajökull to IS18 path. The maxima in signal amplitude and apparent speed at ~13:00 UT occur at times of maximum stratospheric ducting (Figure 12). At these times of high $\Phi_{50,1.5}$ numerical modeling predicts that infrasound from a wider swath of takeoff angles at the source is trapped in the stratospheric acoustic duct. Therefore, larger numbers of rays are predicted to arrive at the receiver, in phase with observed amplitude variations (Figure 9c). In addition, because this additional trapped energy returns at steeper angles with respect to the horizontal, the mean apparent signal speed increases. As argued for the Eyjafjallajökull to IS18 path, the diurnal variations in signal amplitude and apparent speed are difficult to reconcile with possible diurnal variability at the source or receiver.

[54] The maximum observed signal bandwidth does not occur simultaneously with the maximum signal amplitudes, as it does along the Eyjafjallajökull to IS18 path. Moreover, along the Eyjafjallajökull to BKNI path the maximum

observed bandwidth occurs at times close to the minimum noise levels (Figure 12), which suggests that the weak variations in signal bandwidth are controlled by diurnal variations in near-receiver noise. In addition, the small changes in bandwidth do not significantly influence the signal amplitude variations which, as discussed above, appear to be controlled by changes in stratospheric ducting efficiency. One factor contributing to this is the large amplitude microbarom noise recorded at BKNI which masks any low-amplitude volcanic signals at frequencies below ~0.3 Hz. It is the observation of these low frequencies that cause the large bandwidth variations recorded at IS18 (Appendix A).

[55] The diurnal variations of up to 4° in observed back azimuth along the Eyjafjallajökull to BKNI path (Figure 4) are difficult to explain. Ray tracing simulations suggest that the stratospheric diurnal variations have little effect on the back azimuth values (Figure 10) and that this is a combination of two factors. First, the path length through the diurnally varying stratosphere (altitudes >45 km) accounts for <10% of the total path length, and second, the variable crosswinds throughout the upper troposphere and lower stratosphere (5 to 40 km altitude) are of comparable amplitude to those at the stratopause. Due to the longer path length in the regions below the stratopause, crosswinds in these regions dominate the predicted back azimuth variations.

[56] However, strong diurnal back azimuth variations are observed; if these variations are associated with diurnal variations at the stratopause, it would be expected that they would be in phase with the diurnal crosswind variations at these altitudes. Along the Eyjafjallajökull to BKNI path the maximum crosswinds at 50 km occur at ~15:00 UT whereas minimum crosswinds occur at ~00:00 UT (Figure 10a), compared to the observed variations where maximum back azimuth deviations occur at ~12:00 UT and minimum variations occur at ~01:00 UT. Although the phases of the predicted and observed variations differ by up to 3 h, in both cases the back azimuth variations lag the amplitude variations by 6 h as would be expected from theoretical considerations of the tidal zonal and meridional wind components [*Forbes and Groves*, 1990].

[57] Combining the observations from the two geographically distinct paths to BKNI and IS18, the diurnal variations in amplitude and apparent speed can be explained by one physical mechanism: stratospheric effective sound speed variations caused by stratospheric tidal motions. Changes in signal frequency content are explained by variations in signal-to-noise ratio: at IS18 it is the variability in recorded signal power that causes the bandwidth changes while at BKNI diurnal changes in the ambient noise amplitude drive the SNR variations. At present, diurnal variations in back azimuth along the Eyjafjallajökull to BKNI path are unexplained.

7. Discussion

7.1. Comparison to Previous Studies

[58] The study of signals from Eyjafjallajökull differs from many of the previous infrasound studies of diurnal variations as it concentrates on variability close to the stratopause, instead of within the more variable mesosphere and lower thermosphere [e.g., *Donn and Rind*, 1971; *Rind and Donn*, 1975; *Assink et al.*, 2012]. The few studies that suggest an influence of stratospheric solar tides on infrasound propagation [*Donn and Rind*, 1971, 1972] suffer from lack of knowledge with regards the source (microbarom) location and were conducted prior to the advent of sophisticated numerical weather prediction hindcast models.

[59] The eruption of Eyjafjallajökull, an example of a precisely located quasi-continuous volcanic infrasound source, provided excellent temporal data coverage. This allowed the diurnal variations within the data to be interpreted alongside the sophisticated ECMWF numerical hindcasts (section 4) and the acoustic propagation modeling (section 5). Our study confirms the findings of *Donn and Rind* [1971, 1972] that stratospheric solar tides can generate observable diurnal variations in signal amplitude. In addition, by analyzing the frequency content of the signals it is shown that the amplitude changes of the signal are also dependent upon the observable bandwidth.

[60] The study presented here would have been improved if local measurements (at ranges <50 km) had been made during the most active phase of the Eyjafjallajökull eruption, such as those available to *Assink et al.* [2012] in their study of signals generated by Tungurahua volcano, Ecuador. Local measurements may have allowed absolute travel times to have been calculated, which *Assink et al.* [2012] used to provide constraints on thermospheric tidal motions. However, this would depend on the ability to correlate local recordings of a quasi-continuous source with measurements made at distances greater than 1700 km. This is a nontrivial task as arrivals from sources temporally separated by hundreds of seconds can overlap, as shown by *Green et al.* [2011] for accidental munitions explosions.

[61] Looking ahead to broader studies, the Eyjafjallajökull source would be unsuitable for continuous atmospheric monitoring; the signals quickly waned after the initial high-intensity eruptive phase. Volcanoes such as Yasur, Vanuatu, may be more suited to such studies as they generate long time series (months to years) of frequent (up to several hundred per day), detectable explosions; recent preliminary studies suggest well constrained measurements of tidal variations can be made using infrasound generated at this source [*Dalaudier et al.*, 2009].

7.2. Implications

[62] The Eyjafjallajökull infrasound signals have provided an opportunity to assess the effect of stratospheric tidal motions on acoustic propagation over ranges ≥1500 km. The results show that stratospheric tidal variations can generate rapid variations (with timescales on the order of an hour) in observable infrasound parameters. Therefore, tidal contributions need to be assessed alongside gravity wave and wind shear [e.g., *Kulichkov*, 2004] when considering short timescale variations in infrasonic stratospheric returns.

[63] The interpretation of diurnal variations in this study also clearly indicates the requirement to account for along-path variations in effective sound speed when modeling infrasonic returns; range-independent modeling fails to predict the observed diurnal variations. This is because the efficiency of acoustic ducting over paths with many stratospheric bounces is controlled by the weakest part of the duct (i.e., where $\Phi_{stratosphere,source}$ is lowest); variations at the weakest location can be masked by averaging the effective sound speed over a long path. The importance of range-dependent effects has implications for studies of infrasound network detection capability. Along-path mean stratospheric wind speeds were used to predict infrasonic amplitudes at distant stations in recent models of the global network being installed as part of the verification measures for a Comprehensive Nuclear Test ban Treaty [*Le Pichon et al.*, 2009; *Green and Bowers*, 2010]. The results presented in this paper suggest that it is the minimum along-path stratospheric wind speeds that control the recorded amplitude at distant stations.

[64] The results presented here also have implications for studies where infrasound signal amplitudes and bandwidths recorded at long ranges (e.g., >400 km) are used to assess source size and source dynamics. For example, the estimation of chemical (and nuclear) explosive yield using infrasound relies on measurements of signal bandwidth and amplitude [e.g., *Whitaker et al.*, 2003; *Edwards et al.*, 2006]. As discussed above, the results of the Eyjafjallajökull study suggest that for propagation over long paths the region of weakest stratospheric ducting will control the amplitude of the signal reaching the station. This effect should be considered in any future yield determination tools designed to use long-range infrasound. In addition, this study shows that for signals with low signal-to-noise ratios the efficiency of acoustic ducting can significantly influence the recorded signal bandwidth and amplitude. In terms of tidal variability it is expected that at times when the stratospheric solar tide acts to increase the minimum along-path $\Phi_{stratosphere,source}$ the bandwidth and amplitude of the signal will be increased, such that the source will appear to be larger than if recorded when tidal variations act to reduce $\Phi_{stratosphere,source}$.

[65] An example of interest is the often used infrasound amplitude versus explosive yield relationship developed at Los Alamos [*Whitaker et al.*, 2003]. The relationship is derived from observations of chemical explosions in the U.S. The majority, if not all, of these explosions occurred
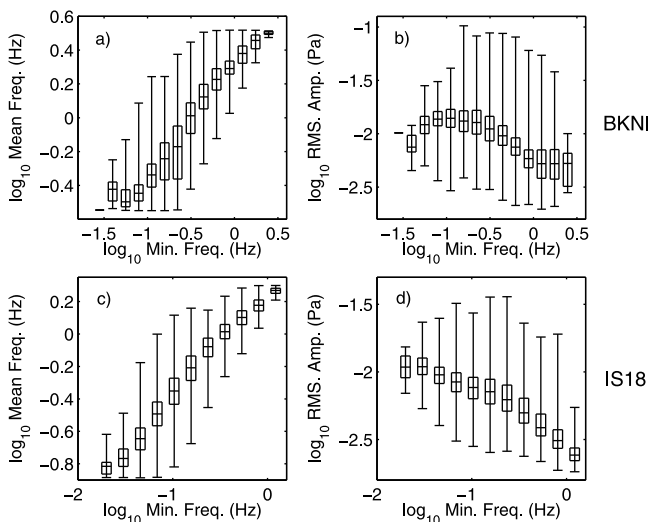
Figure A1. (a and c) The relationship between the minimum frequency band of detection and both the mean frequency of detection and (b and d) the RMS signal amplitude. The spread of values are shown using standard box plots; the horizontal lines from bottom to top represent the sample minimum, the lower quartile, the median, the upper quartile and the sample maximum, respectively. The results are for the time period 00:00 UT 18 April 2010 to 00:00 UT 28 April 2010. The minimum frequency values at which the results are binned correspond to the logarithmically spaced frequency bands used within the PMCC detection algorithm.

during the morning or early afternoon (local time) in a limited geographical area [see *Warshaw and Dubois*, 1981; *Mutschlecner and Whitaker*, 1987; *Evinrude*, 1986; *Lehr*, 1987; *Davidson and Whitaker*, 1992; *Howe*, 1996; *Bhattacharyya et al.*, 2003]. Therefore, the empirical relationships do not account for any signal changes that occur due to the diurnal cycle.

[66] Changes in infrasound signal frequency content with time also have implications for using infrasound signals within systems designed to reduce the risks to aviation from volcanic hazards [e.g., *Garcés et al.*, 2008]. It has been shown that infrasound signals associated with eruptions producing sustained, tall ash plumes contain significant power at low (<0.5 Hz) frequencies [e.g., *Fee et al.*, 2010]. Recent work has shown that this energy can be detected at ranges of thousands of kilometers, and that there is a relationship, albeit weak, between the low-frequency signal power and plume height [*Dabrowa et al.*, 2011]. However, as the study of signals from Eyjafjallajökull shows, especially on the propagation path to IS18, significant increases in low-frequency signal power over timescales of hours can be attributed to propagation conditions. Therefore, if remote infrasound data are to be used in hazard mitigation systems, acoustic propagation variability will need to be accounted for in order to isolate variations due to source processes.

[67] The Eyjafjallajökull data set also shows that infrasound propagation is sensitive to low-amplitude (<20 m/s) tidal variations in wind speed close to the stratopause, and provides a further example of how infrasound recordings may contribute to the validation of stratospheric dynamics

models [e.g., *Kulichkov*, 2004; *Le Pichon et al.*, 2006; *Evers and Siegmund*, 2009]. For studies of the stratospheric solar tides infrasound measurements may provide an opportunity for measuring local variations in tidal strength, and the interaction of tidal motions with other meteorological phenomena such as planetary waves [e.g., *Lieberman et al.*, 2004].

[68] However, the Eyjafjallajökull eruption data set is not ideal for quantitative studies of stratospheric variability. Because the source-to-receiver path lengths are long (>1500 km), and as the signal variations are the result of integrating C_{eff} changes along the entire path, it is difficult to isolate variations generated close to the stratopause. In addition to significant range-dependent meteorology, the meteorological conditions change over the timescales (of hours) required for infrasound propagation over thousands of kilometers. Therefore, future studies of how stratospheric solar tides influence infrasound propagation would benefit from using regional recordings (at ranges <400 km); such recordings may provide well constrained quantitative estimates of stratospheric tidal variability [e.g., *Dalaudier et al.*, 2009].

[69] Detailed acoustic studies of stratospheric tides will require microbarograph arrays whose geometry and aperture are optimized to provide suitable resolution in wavefront parameter estimates. The kilometer-scale eight-sensor arrays of global monitoring stations such as IS18 provide a good compromise between retaining signal coherency across the array and parameter estimate resolution (<3° in azimuth and <20 m/s in apparent speed). In addition, an infrasound array local to the source (at ranges <20 km) is always a valuable resource. As shown by *Assink et al.* [2012], a local array allows variations in travel time to be measured, providing extra constraints for atmospheric parameter inversions. Local recordings would also provide better constraints on the source spectrum for amplitude and bandwidth studies.

8. Concluding Remarks

[70] Quasi-continuous recordings of infrasound signals at long-range (>1500 km) generated by the summit eruption of Eyjafjallajökull volcano, Iceland, exhibit statistically significant diurnal variations in amplitude, frequency bandwidth, apparent speed, and back azimuth. The magnitude and phase of the variations are path dependent.

[71] The diurnal variations in infrasound signal amplitude and apparent speed can be attributed to the diurnal strengthening and weakening of the stratospheric acoustic duct, in response to variations in along-path wind speeds generated by the stratospheric solar tides. In order to model the observed diurnal variations, range-dependent meteorology is required; propagation modeling using averaged meteorological profiles fails to predict the leakage of acoustic energy out of the stratospheric acoustic duct at times of low observed signal amplitudes.

[72] Diurnal variations in signal bandwidth are due to two independent factors that act to change the signal-to-noise ratio. First, an increase in acoustic duct strength, due to diurnal tidal wind strengthening in the stratosphere can increase the signal-to-noise ratio. Second, diurnal variations in incoherent ambient noise at the receiver, due to diurnal variations in near-ground turbulence, can reduce the noise at nighttime and

consequently increase the signal-to-noise ratio and signal detectability. Both of these effects are frequency dependent.

[73] Currently the observed diurnal back azimuth variations between Eyjafjallajökull and BKNI cannot be explained (no significant back azimuth variations were observed between Eyjafjallajökull and IS18); numerical propagation modeling along both the Eyjafjallajökull to BKNI and IS18 paths predict no diurnal back azimuth variations.

[74] The results confirm that infrasound recordings at long ranges (>1500 km) are sensitive to the <20 m/s diurnal variations in wind speed generated by stratospheric solar tides. In future studies of stratospheric dynamics, infrasound may prove to be a useful tool in helping validate models of stratospheric tidal variability. Strong range dependence in the ducting of stratospheric infrasound makes it difficult to quantitatively predict the influence of the stratospheric tides on the wavefront properties observed at long ranges. Therefore, it would likely be more straightforward to identify and model stratospheric tidal signatures in regional infrasound recordings (ranges <400 km) from a quasi-continuous source.

Appendix A: The Relationship Between Signal Bandwidth and Amplitude

[75] In section 2 the mean signal frequency at IS18 was shown to exhibit an inverse relationship with the signal bandwidth (Figure 3): when the signal contains lower frequencies, or equivalently the signal bandwidth increases, the mean frequency decreases. As expected, when the signal bandwidth increases the signal amplitude increases due to the increased detectable power (Figures 13 and A1d).

[76] At IS18 this variation in detectable power with signal bandwidth is particularly strong (Figures 3e and 3h), and is a consequence of the volcanic signal bandwidth spanning the microbarom peak (Figure 13). At times of low volcanic signal power the ambient noise levels associated with the microbarom source prevent the observation of any lower-frequency volcanic signals (Figure 13a). As the signal power increases the volcanic signal can be seen above the microbarom peak extending the observed signal bandwidth down to below 0.1 Hz (Figures 13b–13d), and therefore dramatically increasing the observed signal power and hence amplitude (Figure 3e). It is also observed that the power at the microbarom peak increases in the same time periods as the volcanic signal power does (Figure 13e); this would be expected if the acoustic duct is strengthening, increasing both volcanic and microbarom signal transmission.

[77] Although a strong negative correlation between signal amplitude and mean signal frequency is not observed at BKNI (Figure 3), the relationships between lowest detectable frequency, mean signal frequency and RMS amplitude exhibit the same patterns as at IS18 (Figures A1a and A1b), although the reduction of RMS amplitude with decreased bandwidth is less pronounced. One cause of the weaker relationship at BKNI is that the volcanic signal is rarely observed at frequencies less than 0.3 Hz. Only 6% of Eyjafjallajökull associated detections at BKNI have energy below 0.3 Hz, compared to 75% of detections at IS18. This suggests that at BKNI any lower-frequency portion of the volcanic signal is not of high enough amplitude to be seen above the microbarom peak, or that the smaller aperture

(∼200 m) BKNI array cannot resolve between the two sources at these frequencies.

References

Arrowsmith, S. J., D. P. Drob, M. A. H. Hedlin, and W. Edwards (2007), A joint seismic and acoustic study of the Washington State bolide: Observations and modeling, *J. Geophys. Res.*, *112*, D09304, doi:10.1029/2006JD008001.

Assink, J. D., R. Waxler, and D. Drob (2012), On the sensitivity of infrasonic travletimes in the equatorial region to the atmospheric tides, *J. Geophys. Res.*, *117*, D01110, doi:10.1029/2011JD016107.

Baisch, S., and G. H. R. Bokelmann (1999), Spectral analysis with incomplete time series: An example from seismology, *Comput. Geosci.*, *25*, 739–750, doi:10.1016/S0098-3004(99)00026-6.

Balachandran, N. K., W. J. Donn, and G. Kaschak (1971), On the propagation of infrasound from rockets: Effects of winds, *J. Acoust. Soc. Am.*, *50*(2), 397–404.

Bhattacharyya, J., H. Bass, D. Drob, R. Whitaker, D. Revelle, and T. Sandoval (2003), Description and analysis of infrasound and seismic signals recorded from the Watusi explosive experiment, September 2002, paper presented at 25th Annual Seismic Research Symposium, U.S. Dep. of Energy, Tuscon, Ariz.

Brachet, N., D. Brown, R. Le Bras, P. Mialle, and J. Coyne (2010), Monitoring the Earth's atmosphere with the global IMS Infrasound Network, in *Infrasound Monitoring for Atmospheric Studies*, edited by A. Le Pichon, E. Blanc, and A. Hauchecorne, pp. 77–118, Springer, Dordrecht, Netherlands.

Cansi, Y. (1995), An automatic seismic event processing for detection and location: The P.M.C.C. Method, *Geophys. Res. Lett.*, *22*, 1021–1024, doi:10.1029/95GL00468.

Collins, M. D. (1993), A split-step Padé solution for the parabolic equation method, *J. Acoust. Soc. Am.*, *93*(4), 1736–1742, doi:10.1121/1.406739.

Dabrowa, A., D. N. Green, A. Rust, and J. C. Phillips (2011), A global study of volcanic infrasound characteristics and the potential for long-range monitoring, *Earth Planet. Sci. Lett.*, *310*, 369–379.

Dalaudier, F., A. Le Pichon, A. Hauchecorne, E. Blanc, and C. Cot (2009), Quantification of wind and diurnal tide in the upper stratosphere—Prospective for assimilation, in *Geophys. Res. Abstr.*, *11*, 8364.

Davidson, M., and R. W. Whitaker (1992), Miser's gold, *Tech. Rep. LA-12074-MS*, Los Alamos Natl. Lab., Los Alamos, N. M.

Dessa, J.-X., J. Virieux, and S. Lambotte (2005), Infrasound modeling in a spherical heterogeneous atmosphere, *Geophys. Res. Lett.*, *32*, L12808, doi:10.1029/2005GL022867.

Donn, W. L., and D. Rind (1971), Natural infrasound as an atmospheric probe, *Geophys. J. R. Astron. Soc.*, *26*, 111–133.

Donn, W. L., and D. Rind (1972), Microbaroms and the temperature and wind of the upper atmosphere, *J. Atmos. Sci.*, *29*, 156–172.

Drob, D. P., J. M. Picone, and M. Garcs (2003), Global morphology of infrasound propagation, *J. Geophys. Res.*, *108*(D21), 4680, doi:10.1029/2002JD003307.

Drob, D. P., et al. (2008), An empirical model of the Earth's horizontal wind fields: HWM07, *J. Geophys. Res.*, *113*, A12304, doi:10.1029/2008JA013668.

Drob, D. P., M. Garcés, M. Hedlin, and N. Brachet (2010), The temporal morphology of infrasound propagation, *Pure Appl. Geophys.*, *167*, 437–453.

Edwards, W. N., and D. N. Green (2012), Effect of interarray elevation differences on infrasound beamforming, *Geophys. J. Int.*, *190*, 335–346, doi:10.1111/j.1365-246X.2012.05465.x.

Edwards, W. N., P. G. Brown, and D. O. ReVelle (2006), Estimates of meteoroid kinetic energies from observations of infrasonic airwaves, *J. Atmos. Sol. Terr. Phys.*, *68*, 1136–1160.

Evers, L. G., and H. W. Haak (2005), The detectibility of infrasound in The Netherlands from the Italian volcano Mt. Etna, *J. Atmos. Sol. Terr. Phys.*, *67*, 259–268, doi:10.1016/j.jastp.2004.09.002.

Evers, L. G., and H. W. Haak (2010), The characteristics of infrasound, its propagation and some early history, in *Infrasound Monitoring for Atmospheric Studies*, edited by A. Le Pichon, E. Blanc, and A. Hauchecorne, pp. 3–28, Springer, Dordrecht, Netherlands.

Evers, L. G., and J. Schweitzer (2011), A climatology of infrasound dectections in northern Norway at the experimental ARCI array, *J. Seismol.*, *15*, 473–486, doi:10.1007/s10950-011-9237-8.

Evers, L. G., and P. Siegmund (2009), Infrasonic signature of the 2009 major sudden stratospheric warming, *Geophys. Res. Lett.*, *36*, L23808, doi:10.1029/2009GL041323.

Evinrude, M. G. (1986), Minor Scale Event: Test Execution Report, *Tech. Rep. POR 7157*, Def. Nucl. Agency, Washington, D. C.

Fee, D., and M. Garcs (2007), Infrasonic tremor in the diffraction zone, *Geophys. Res. Lett.*, *34*, L16826, doi:10.1029/2007GL030616.D00L10

Fee, D., A. Steffke, and M. Garcés (2010), Characterization of the 2008 Kasatochi and Okmok eruptions using remote infrasound arrays, *J. Geophys. Res.*, *115*, D00L10, doi:10.1029/2009JD013621.

Forbes, J. M. (1987), Modelling the propagation of atmospheric tides from the lower to the middle and upper atmosphere, *Phys. Scr. T*, *18*, 240–248.

Forbes, J. M. (1990), Atmospheric tides between 80 km and 120 km, *Adv. Space Res.*, *10*(12), 127–140.

Forbes, J. M., and G. V. Groves (1990), Atmospheric tides below 80 km, *Adv. Space Res.*, *10*(12), 119–125.

Garcés, M., et al. (2008), Capturing the acoustic fingerprint of stratospheric ash injection, *Eos Trans. AGU*, *89*(40), 377–378.

Garratt, J. R. (1992), *The Atmospheric Boundary Layer*, Cambridge Univ. Press, Cambridge, U. K.

Green, D. N., and D. Bowers (2010), Estimating the detection capability of the International Monitoring System infrasound network, *J. Geophys. Res.*, *115*, D18116, doi:10.1029/2010JD014017.

Green, D. N., J. Vergoz, R. Gibson, A. Le Pichon, and L. Ceranna (2011), Infrasound radiated by the Gerdec and Chelopechene explosions: Propagation along unexpected paths, *Geophys. J. Int.*, *185*, 890–910, doi:10.1111/j.1365-246X.2011.04975.x.

Gudmundsson, M. T., R. Pedersen, K. Vogfjörd, B. Thorbjarnardóttir, S. Jakobsdóttir, and M. J. Roberts (2010), Eruptions of Eyjafjallajökull Volcano, Iceland, *Eos Trans. AGU*, *91*(21), 190–191.

Hagerty, M. T., W.-Y. Kim, and P. Martysevich (2002), Infrasound detection of large mining blasts in Kazakstan, *Pure Appl. Geophys.*, *159*(5), 1063–1079.

Hedin, A. E. (1991), Extension of the MSIS thermosphere model into the middle and lower atmosphere, *J. Geophys. Res.*, *96*, 1159–1172.

Heslop, D., and M. J. Dekkers (2002), Spectral analysis of unevenly spaced climatic time series using CLEAN: Signal recovery and derivation of significance levels using a Monte Carlo simulation, *Phys. Earth Planet. Inter.*, *130*, 103–116.

Howe, J. S. (1996), The measurement of airblast parameters on the Minor Uncle explosion event using passive instrumentation, *Tech. Rep. DSTO-TN-0035*, Def. Sci. and Technol. Org., Canberra, Australia.

Kulichkov, S. N. (2004), Long-range propagation and scattering of low-frequency sound pulses in the middle atmosphere, *Meteorol. Atmos. Phys.*, *85*, 47–60.

Kulichkov, S. N., and G. A. Bush (2001), Rapid variations of the infrasonic signals at long distances from one-type exploisons, *Izv. Atmos. Oceanic Phys.*, *37*(3), 306–313.

Kulichkov, S. N., I. P. Chunchuzov, and O. I. Popov (2010), Simulating the influence of an atmospheric fine inhomogeneous structure on long-range propagation of pulsed acoustic signals, *Izv. Atmos. Oceanic Phys.*, *46*(1), 60–68.

Lehr, D. (1987), Misty picture event: Test execution report, *Tech. Rep. POR 7186*, Def. Nucl. Agency, Washington, D. C.

Le Pichon, A., E. Blanc, and D. Drob (2005a), Probing high-altitude winds using infrasound, *J. Geophys. Res.*, *110*, D20104, doi:10.1029/2005JD006020.

Le Pichon, A., E. Blanc, D. Drob, S. Lambotte, J. X. Dessa, M. Lardy, P. Bani, and S. Vergniolle (2005b), Infrasound monitoring of volcanoes to probe high-altitude winds, *J. Geophys. Res.*, *110*, D13106, doi:10.1029/2004JD005587.

Le Pichon, A., L. Ceranna, M. Garcés, D. Drob, and C. Millet (2006), On using infrasound from interacting ocean swells for global continuous measurements of winds and temperature in the stratosphere, *J. Geophys. Res.*, *111*, D11106, doi:10.1029/2005JD006690.

Le Pichon, A., J. Vergoz, E. Blanc, J. Guilbert, L. Ceranna, L. Evers, and N. Brachet (2009), Assessing the performance of the International Monitoring System's infrasound network: Geographical coverage and temporal variabilities, *J. Geophys. Res.*, *114*, D08112, doi:10.1029/2008JD010907.

Le Pichon, A., J. Vergoz, Y. Cansi, L. Ceranna, and D. Drob (2010), Contribution of infrasound monitoring for atmospheric remote sensing, in *Infrasound Monitoring for Atmospheric Studies*, edited by A. Le Pichon, E. Blanc, and A. Hauchecorne, pp. 629–646, Springer, Dordrecht, Netherlands.

Lieberman, R. S., J. Oberheide, M. E. Hagan, E. E. Remsberg, and L. L. Gordley (2004), Variability of diurnal tides and planetary waves during November 1978–May 1979, *J. Atmos. Sol. Terr. Phys.*, *66*, 517–528.

Lindzen, R. S., and S. Chapman (1969), Atmospheric tides, *Space Sci. Rev.*, *10*, 3–188.

Matoza, R. S., et al. (2011a), Long-range acoustic observations of the Eyjafjallajökull eruption, Iceland, April–May 2010, *Geophys. Res. Lett.*, *38*, L06308, doi:10.1029/2011GL047019.

Matoza, R. S., A. Le Pichon, J. Vergoz, P. Henry, J.-M. Lalande, H.-I. Lee, I.-Y. Che, and A. Rybin (2011b), Infrasonic observations of the June 2009 Sarychev peak eruption, Kuril Islands: Implications for infrasonic monitoring of remote explosive volcanism, *J. Volcanol. Geotherm. Res.*, *200*(1-2), 35–48, doi:10.1016/j.jvolgeores.2010.11.022.

Mutschlecner, J. P., and R. W. Whitaker (1987), Propagation of near-infrasound over long ranges, *Tech. Rep. LA-UR-87-258*, Los Alamos Natl. Lab., Los Alamos, N. M.

Negraru, P. T., and E. T. Herrin (2009), On infrasound waveguides and dispersion, *Seismol. Res. Lett.*, *80*(4), 565–571.

Neuberg, J. (2000), External modulation of volcanic activity, *Geophys. J. Int.*, *142*, 232–240.

Petersen, G. N. (2010), A short meteorological overview of the Eyjafjallajökull eruption 14 April–23 May 2010, *Weather*, *65*(8), 203–207.

Petersen, G. N., H. Bjornsson, and P. Arason (2012), The impact of the atmosphere on the Eyjafjallajökull 2010 eruption plume, *J. Geophys. Res.*, *117*, D00U07, doi:10.1029/2011JD016762.

Press, W. H., and G. B. Rybicki (1989), Fast algorithm for spectral analysis of unevenly sampled data, *Astrophys. J.*, *338*, 277–280.

Reed, J. W. (1969), Climatology of airblast propagation from Nevada Test Site Nuclear airblasts, *Tech. Rep. SC-RR-69-572*, Sandia Natl. Lab., Albuquerque, N. M.

Rind, D., and W. L. Donn (1975), Further use of natural infrasound as a continuous monitor of the upper atmosphere, *J. Atmos. Sci.*, *32*, 1694–1704.

Roberts, D. H., J. Lehar, and J. W. Dreher (1987), Time series analysis with CLEAN. I. Derivation of a spectrum, *Astron. J.*, *93*(4), 968–989.

Sutherland, L. C., and H. E. Bass (2004), Atmospheric absorption in the atmosphere up to 160 km, *J. Acoust. Soc. Am.*, *115*(3), 1012–1032, doi:10.1121/1.1631937.

Szuberla, C. A. L., and J. V. Olson (2004), Uncertainties associated with parameter estimation in atmospheric infrasound arrays, *J. Acoust. Soc. Am.*, *115*(1), 253–258.

Virieux, J., N. Garnier, E. Blanc, and J.-X. Dessa (2004), Paraxial ray tracing for atmospheric wave propagation, *Geophys. Res. Lett.*, *31*, L20106, doi:10.1029/2004GL020514.

Warshaw, S. I., and P. F. Dubois (1981), Preliminary theoretical acoustic and RF sounding calculations for MILL RACE, *Tech. Rep. UCID-19231*, Lawrence Livermore Natl. Lab., Livermore, Calif.

Whitaker, R. W., T. D. Sandoval, and J. P. Mutschlecner (2003), Recent infrasound analysis, paper presented at 25th Annual Seismic Research Symposium, U.S. Dep. of Energy, Tuscon, Ariz.